

Elsevier required licence: © <2020>. This manuscript version is made available under the CC-BY-NC-ND 4.0 license <http://creativecommons.org/licenses/by-nc-nd/4.0/>

The definitive publisher version is available online at

[\[https://www.sciencedirect.com/science/article/pii/S0307904X20300068?via%3Dihub\]](https://www.sciencedirect.com/science/article/pii/S0307904X20300068?via%3Dihub)

A NURBS-based Multi-Material Interpolation (N-MMI) for Isogeometric Topology Optimization of Structures

Jie Gao^{1,2}, Zhen Luo², Mi Xiao¹, Liang Gao^{1*}, Peigen Li¹

¹ *The State Key Lab of Digital Manufacturing Equipment and Technology, Huazhong University of Science and Technology, 1037 Luoyu Road, Wuhan, Hubei 430074, China*

² *The School of Mechanical and Mechatronic Engineering, University of Technology Sydney, 15 Broadway, Ultimo, NSW 2007, Australia*

* **Corresponding author:** Tel.: +86-27-87557742; E-mail: gaoliang@mail.hust.edu.cn (Prof L. Gao)

Abstract

In this paper, the main intention is to propose a new Multi-material Isogeometric Topology Optimization (M-ITO) method for the optimization of multiple materials distribution, where an improved multi-material interpolation model is developed using Non-Uniform Rational B-splines (NURBS), namely the “NURBS-based Multi-Material Interpolation (N-MMI)”. In the N-MMI model, three key components are involved: (1) multiple Fields of Design Variables (DVs): NURBS basis functions with control design variables are applied to construct DVs with the sufficient smoothness and continuity; (2) multiple Fields of Topology Variables (TVs): each TV is expressed by a combination of all DVs to present the layout of a distinct material in the design domain; (3) multi-material interpolation: the material property at each point is equal to the summation of all TVs interpolated with constitutive elastic properties. DVs and TVs are in the decoupled expression and optimized in a serial evolving mechanism. This feature can ensure the constraint function is separate and linear with respect to TVs, which can be beneficial to reduce the complexity of numerical computations and eliminate numerical troubles in the multi-material optimization. Two kinds of multi-material topology optimization problems are discussed, i.e., one with multiple volume constraints and the other with the total mass constraint. Finally, several numerical examples in 2D and 3D are provided to show the effectiveness of the M-ITO method.

Keywords: Topology optimization; multi-material; Isogeometric analysis; NURBS.

1 Introduction

Topology optimization has undergone significant developments in recent years, because of its capability to find the optimal distribution of materials in the conceptual design phase of products [1]. Up to now, many different methods with the specific characteristics are developed, like the homogenization method [2], the Solid Isotropic Material with Penalization (SIMP) method [3,4], the Evolutionary Structural Optimization (ESO) method [5] and the Level Set Method (LSM) [6–8]. Meanwhile, many complicated problems ranging from the mechanical discipline to other physical fields, have been discussed, e.g. [9–17]. One of them, the multi-material topology optimization provides a new window for the advanced structures, such as cellular composites [13,16,17] etc.

Overall speaking, the multi-material topology optimization problems pose more challenges than the single-material design. The first work might go back to [18], which used the homogenization technique to design a structure with one or two materials. A mixture rule for the interpolation of three-phase material properties was proposed in the framework of the SIMP method to design composites with extreme thermal expansion [19] and extreme bulk modulus [20], which has been also applied to the optimization design of multiphysics actuators [21] and reinforced concrete structures [22]. Stegmann and Lund [23] proposed a discrete material optimization (DMO) to optimize composite laminate shell structures. Then, Gao et al [24,25] extended the mixture rule and DMO to the multi-material problem with the total mass constraint, in which the recursive multiphase materials interpolation (RMMI) model and uniform multiphase materials interpolation (UMMI) model were studied in detail. Two multi-material interpolation schemes as generalizations of the SIMP and RAMP material interpolation schemes were discussed in [26], and the optimization of composite laminated lay-ups was also studied [27]. Later, many multi-material topology optimization methods were developed, such as the peak function to decrease design variables [28], the ordered SIMP interpolation [29], and the alternating active-phase algorithm [30]. [31] developed a continuum topology optimization framework for the multi-material compliance minimization considering arbitrary volume and mass constraints. The LSMs have been also applied to solve several multi-material problems [32,33].

In the multi-material topology optimization, a critical ingredient lies in how to develop an effective multi-material interpolation model. Several challenges will be involved: (1) how to exactly capture each distinct material in a designable element or point; (2) no overlaps: a designable element or point only has a unique phase; (3) no redundant phases: the design domain should be occupied by all materials and the void phase. However, the developed multi-material interpolation models in the previously-mentioned works might not

be effective in some problems. For example, the RMMI model has no capability to ensure the multi-material optimization can seek the optimal design under the total mass constraint [24], where a set of design variables are defined to determine the existence of all materials and other sets work as topology variables to determine the selection of materials. The multi-material topology optimization with the UMMI model might produce the “mixed” materials [24], in which each set of design variables work as the set of topology variables to determine the layout of a unique material. Moreover, a specific feature that design variables and topology variables are expressed in the coupled manner and evolved in a parallel mechanism during the optimization, exists in the above multi-material interpolation models. The coupled expression and parallel evolving cause several numerical issues in the multi-material optimization, like the unrealistic designs with the “mixed” material or a local optimal design [24,34].

On the other side, the numerical analysis in the mentioned-above works are performed by the finite element method (FEM) [35]. Three main drawbacks of the FEM would constrain the effectiveness of the topology optimization: (1) the finite element mesh is only an approximation of the structure [36,37]; (2) the lower-order (C^0) continuity of the structural responses between adjacent finite elements; (3) the lower efficiency to obtain the high quality of the finite element mesh. Isogeometric analysis (IGA), proposed by Hughes and his co-workers [36,37], can be regarded as a logical extension and generalization method of finite element analysis. In IGA, the same basis functions are employed to model the structural geometry and construct the finite dimensional solution space. Hence, no matter how coarse the numerical discretization of the domain is, the structural geometry can be exactly represented. Recently, IGA has been accepted a great number of discussions among many researchers [38,39].

To the best of the authors’ knowledge, the first work of using IGA into the topology optimization might be performed by Seo et al [40], in which the trimmed spline surfaces were applied to represent the boundaries. A phase field model with IGA was developed for the compliance problem [41]. Then, an isogeometrical method to topology optimization was also developed, where the optimality criteria was used to evolve the design variables [42]. Later, Qian [43] constructed a B-spline space for topology optimization and provided a detailed discussion for the B-splines filter. In [44], a unified strategy is developed to simultaneously insert inclusions or holes of regular shape as well as redistribute the material to affect the optimal topologies of solids. IGA has been studied in the framework of LSMs, including an IGA-based parameterized LSM [45], the IGA-based LSM for stress problems [46] and flexoelectric materials [47]. Later, Gao et al [48] proposed a new Isogeometric Topology Optimization (ITO) method, where a density distribution function with the

desired smoothness and continuity was constructed to present the structural topology, and the ITO method with an energy-based homogenization was used to optimize auxetic metamaterials [49]. Hence, it is easily to see that a number of efforts have been devoted to the applications of IGA into topology optimization, but only for the single-material. In terms of the multi-material problems, Lieu and Lee [50] developed an IGA-based multi-material topology optimization method, where the alternating active-phase algorithm was directly used. Taheri and Suresh [34] developed an IGA-based topology optimization method for multiple materials and functionally graded structures, with the direct use of the DMO model. We can easily find that the above discussed numerical troubles of the multi-material interpolation models are still occurred in the optimization. Hence, it is of great importance to develop a more effective multi-material ITO method with the superior capability to seek for the optimal distributions of multiple materials.

In this work, we intend to propose a Multi-Material Interpolation model using NURBS (N-MMI), and then apply it to develop a new Multi-material Isogeometric Topology Optimization (M-ITO) method. In the N-MMI model, two kinds of variables are introduced, including Fields of Design Variables (DVs) and Fields of Topology Variables (TVs). TVs and DVs are expressed in the decoupled manner and optimized in a serial evolving mechanism, rather than the coupled and parallel manner. The decoupled expression and serial evolving of the DVs and TVs can make sure all constraint functions are separate and linear with respect to TVs, which is beneficial to solve multi-material problems, particularly for the problem with the total mass constraint. Finally, the outline of the paper is provided as follows: a brief description about IGA is shown in Section 2 and the N-MMI model is given in Section 3. Two M-ITO formulations are developed in Section 4 using the N-MMI, and sensitivity analysis is derived. Several 2D and 3D numerical examples are performed in Section 5, and the paper ends with the concluding remarks in Section 6.

2 A brief introduction about Isogeometric analysis (IGA)

IGA aims to integrate the computer-aided design (CAD) model with the computer-aided engineering (CAE) analysis model in an integrated mathematical form [36,37]. NURBS, which is the standard computational geometry technology in industry [51], are employed in the current work.

2.1 NURBS for geometrical model and spatial discretization

The geometrical model of structures is constructed by a linear approximation of the NURBS basis functions with a set of control points, Given that a control net of points $\mathbf{P}_{i,j} \in \mathbb{R}^2$ ($i = 1, 2, \dots, n; j = 1, 2, \dots, m$), the mathematical form of a tensor product NURBS surface $\mathbf{S}(\xi, \eta)$ is defined as:

$$\mathbf{S}(\xi, \eta) = \sum_{i=1}^n \sum_{j=1}^m R_{i,j}^{p,q}(\xi, \eta) \mathbf{P}_{i,j} \quad (1)$$

where n and m are the numbers of control points in two parametric directions, respectively. ξ and η are two normal parametric directions, respectively. p and q indicate the polynomial orders of basis functions, respectively. R are the bivariate NURBS basis functions expressed by the B-spline basis functions:

$$R_{i,j}^{p,q}(\xi, \eta) = \frac{N_{i,p}(\xi)M_{j,q}(\eta)\omega_{ij}}{\sum_{i=1}^n \sum_{j=1}^m N_{i,p}(\xi)M_{j,q}(\eta)\omega_{ij}} \quad (2)$$

where ω_{ij} is the positive weight assigned to the control point $\mathbf{P}_{i,j}$. $N_{i,p}$ and $M_{j,q}$ indicate the univariate B-spline basis functions in two parametric directions ξ and η , respectively. The B-spline basis function is defined by the Cox-de-Boor formula [52], and the recursive formula in ξ direction with a non-decreasing knot vector $\Xi = \{\xi_1, \xi_2, \dots, \xi_{n+p+1}\}$ is defined, starting from $p = 0$:

$$N_{i,0}(\xi) = \begin{cases} 1 & \text{if } \xi_i \leq \xi_{i+1} \\ 0 & \text{otherwise} \end{cases} \quad (3)$$

For $p \geq 1$, the basis functions are defined by

$$N_{i,p}(\xi) = \frac{\xi - \xi_i}{\xi_{i+p} - \xi_i} N_{i,p-1}(\xi) + \frac{\xi_{i+p+1} - \xi}{\xi_{i+p+1} - \xi_{i+1}} N_{i+1,p-1}(\xi) \quad (4)$$

It should be noted that the fractions with the form 0/0 in Eq. (4) are defined as zero. Similarly, the basis functions $M_{j,q}$ in the η direction are also defined by Eqs. (3) and (4). NURBS basis functions are featured with several important properties [36,51]: (1) **Nonnegativity**: $N_{i,p}(\xi) \geq 0$; (2) **Local support**: The support of each basis function $N_{i,p}$ is contained in the interval $[\xi_i, \xi_{i+p+1}]$; (3) **Partition of unity**: For an arbitrary knot span $[\xi_i, \xi_{i+1}]$, $\forall \xi \in [\xi_i, \xi_{i+1}]$, $\sum_{j=i-p}^i N_{j,p}(\xi) = 1$; (4) **Continuity**: C^{p-k} , k is the multiplicity of the knots. As an example shown in **Fig. 1**, a quarter annulus is constructed by the NURBS basis functions

with a set of the control points plotted by red dots, where the structural geometry is displayed in **Fig. 1 (a)**. The NURBS-based geometrical model (CAD) and the discretized IGA mesh for numerical analysis (CAE) are shown in **Fig. 1 (b)** and (c), respectively. The final integration of CAD and CAE is illustrated in **Fig. 1 (g)**, and the corresponding basis functions in two parametric directions are indicated in **Fig. 1 (d)** and (e). The bivariate NURBS basis functions are displayed in **Fig. 1 (f)**.

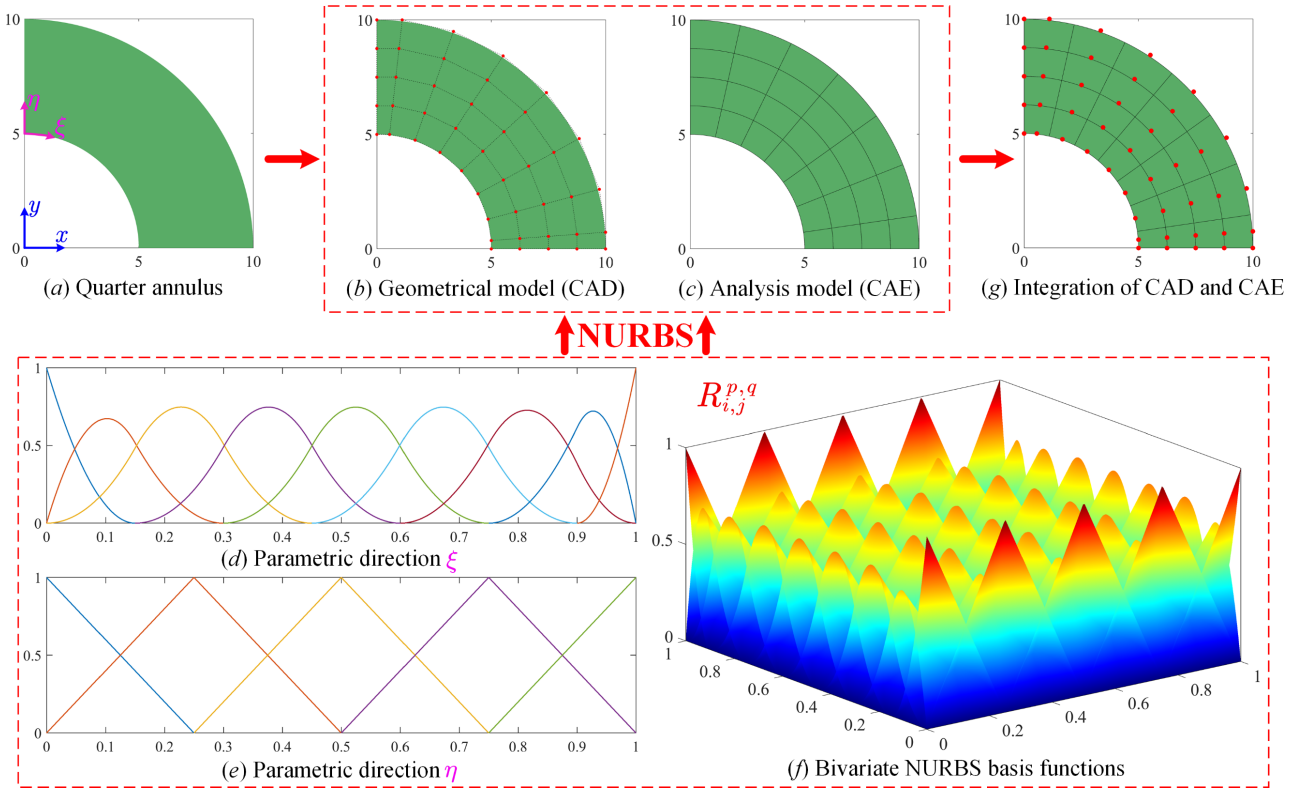


Fig. 1. NURBS surface for a quarter annulus: $\Xi = \{0,0,0,0.15, \dots, 0.90,1,1,1\}$, $\mathcal{H} = \{0,0,0.25,0.5,0.75,1,1\}$; $n = 9, m = 5$; $p = 2, q = 1$.

2.2 Numerical discretization in IGA

In IGA, the NURBS basis functions are firstly applied to model the structural geometry, and then construct the solution space for structural responses. The solution space is defined by a linear combination of NURBS basis functions and responses at control points. The corresponding equation is consistent with Eq. (1), but control coefficients correspond to responses of control points, expressed by:

$$\mathbf{U}(\xi, \eta) = \sum_{i=1}^n \sum_{j=1}^m R_{i,j}^{p,q}(\xi, \eta) \mathbf{U}_{i,j} \quad (5)$$

where \mathbf{U} denotes the field of structural responses in design domain, and $\mathbf{U}_{i,j}$ is the structural response at the control point $\mathbf{P}_{i,j}$.

In the current work, the linear elasticity is considered here only for the sake of the numerical simplicity but without losing any generality. In the Galerkin IGA formulation, the system stiffness matrix and load vector are obtained by assembling the local stiffness matrix and local load vector, respectively. As shown in **Fig.**

2 (a), the quarter annulus is discretized by a series of IGA elements which correspond to knot spans in the parametric space. The IGA element stiffness matrix is computed by Gauss quadrature method, and the iso-parametric formulation is applied to calculate the element stiffness matrix, given as:

$$\mathbf{K}_e = \sum_{i=1}^3 \sum_{j=1}^3 \{ \mathbf{B}^T(\xi_i, \eta_j) \mathbf{D} \mathbf{B}(\xi_i, \eta_j) |J_1(\xi_i, \eta_j)| |J_2(\xi_i, \eta_j)| w_i w_j \} \quad (6)$$

where \mathbf{B} is the strain-displacement matrix calculated by the partial derivatives of the basis functions with respect to physical coordinates. As displayed in Fig. 2, a mapping $\mathbf{X}: \widehat{\Omega}_e \rightarrow \Omega_e$ from the parametric space to the physical space and an affine mapping $\mathbf{Y}: \widetilde{\Omega}_e \rightarrow \widehat{\Omega}_e$ from the bi-unit parent element to the parametric element are defined. J_1 and J_2 are Jacobi matrices of these two mappings, respectively. w_i and w_j are the corresponding quadrature weights. As shown in Fig. 2, all the Gauss quadrature points in the IGA mesh and a 3×3 quadrature points in an IGA element are shown.

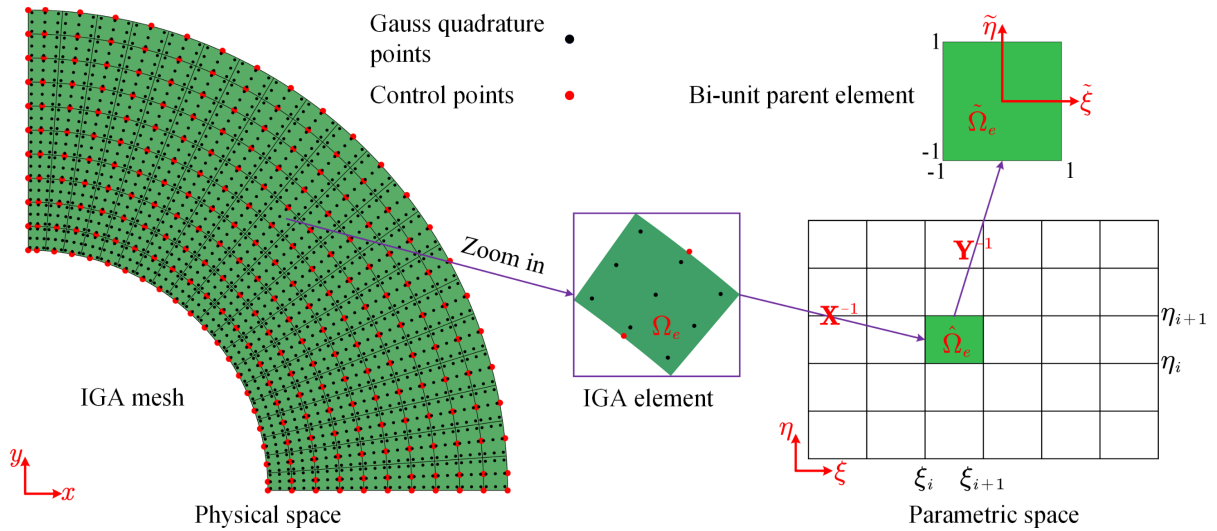


Fig. 2. Quarter annulus: IGA mesh with Gauss quadrature points

3 NURBS-based Multi-Material Interpolation (N-MMI)

In terms of a multi-material topology optimization problem, it is assumed that θ distinct materials need to be distributed in the design domain. we should introduce θ Fields of Topology Variables (TVFs) ϕ^ϑ ($\vartheta = 1, 2, \dots, \theta$), each of field determines the layout of a unique material. In order to define the TVFs, θ Fields of Design Variables (DVs) \mathcal{X}^ϑ are introduced in the design domain, and each TVF is defined by a combination of all DVs.

3.1 The Field of Design Variables (DVF)

The DVs are employed to construct the TVFs, and two basic requirements should be maintained to ensure the justified topology variables: 1) Nonnegativity; 2) Strict bounds. we can see that two conditions are same as the introducing of nodal densities to define the topology in [53–55]. The DVF is constructed by NURBS

basis functions linearly combined with control design variables, and each control design variable is assigned to a control point. As shown in **Fig. 3 (a)**, control points are plotted with the red color. Control design variables are varied in a strict bound $[0, 1]$, given in **Fig. 3 (b)**, and the DVF is shown in **Fig. 3 (c)**.

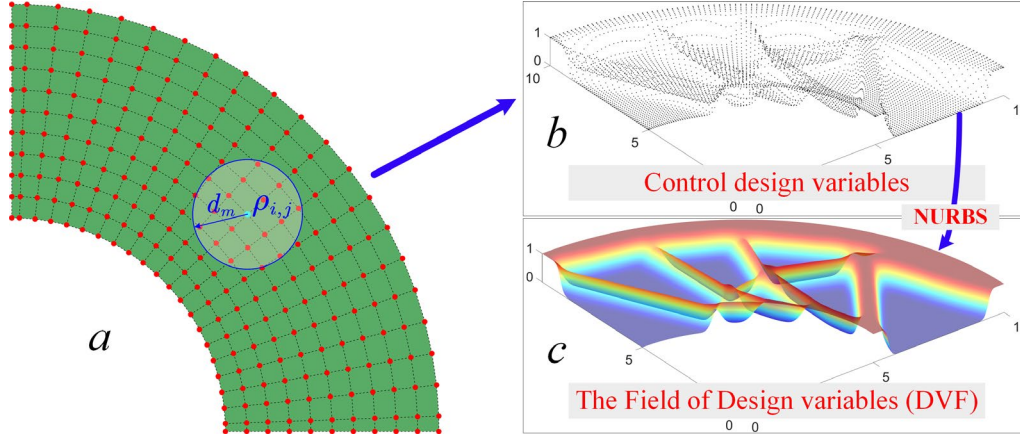


Fig. 3. The construction of the DVF

3.1.1 Smooth control design variables using Shepard function

As discussed in [48,49], the smoothness mechanism plays a significant but different role in the optimization compared to the filtering [56]. The smoothness of control design variables should be enhanced to make sure the DVF with the desired smoothness. The principle is that each control design variable is equal to the mean value of all design variables in the local support area of the current design variable, as shown in the circular area of **Fig. 3 (a)**, explicitly expressed as:

$$\mathcal{G}(\rho_{i,j}) = \sum_{i=1}^{\mathcal{N}} \sum_{j=1}^{\mathcal{M}} \psi(\rho_{i,j}) \rho_{i,j} \quad (7)$$

where $\mathcal{G}(\rho_{i,j})$ is the smooth design variable at the $(i,j)_{th}$ control point, and $\rho_{i,j}$ is the initial variable which needs to satisfy the nonnegative and range-bound $[0, 1]$. \mathcal{N} and \mathcal{M} denote the numbers of control design variables in the local support area with two parametric directions, respectively. $\psi(\rho_{i,j})$ is the value of the Shepard function [57] at the $(i,j)_{th}$ control design variable, and given by:

$$\psi(\rho_{i,j}) = \varphi(\rho_{i,j}) / \sum_{i=1}^{\mathcal{N}} \sum_{j=1}^{\mathcal{M}} \varphi(\rho_{i,j}) \quad (8)$$

where $\varphi(\rho_{i,j})$ is the weight value of the $(i,j)_{th}$ control design variable, and it can be defined by several functions. Here, the compactly supported RBFs with the C^4 continuity are used here due to the compactly supported, high-order continuity and nonnegativity, as:

$$\varphi(r) = (1 - r)_+^6 (35r^2 + 18r + 3) \quad (9)$$

where $r = d/d_m$. d denotes the Euclidean distance between the current control design variable and the other variable in the local support area. d_m is the radius of the local area.

3.1.2 Construction of the DVF

Assuming that the DVF is denoted by $\mathcal{X}(\xi, \eta)$, and the mathematical formula is defined by:

$$\mathcal{X}(\xi, \eta) = \sum_{i=1}^n \sum_{j=1}^m R_{i,j}^{p,q}(\xi, \eta) \mathcal{G}(\rho_{i,j}) \quad (10)$$

We can find that Eq. (10) for the DVF has the same form of NURBS surface in Eq. (1). The difference lies in physical meanings of control coefficients. The NURBS surface is transformed into the definition of the DVF for the design domain. The properties 1 to 3 of NURBS basis functions can guarantee the DVF with the nonnegativity and Strict bounds from 0 to 1. The most important aspect is that the variation diminishing property of NURBS can ensure the non-oscillatory of the DVF [36,37].

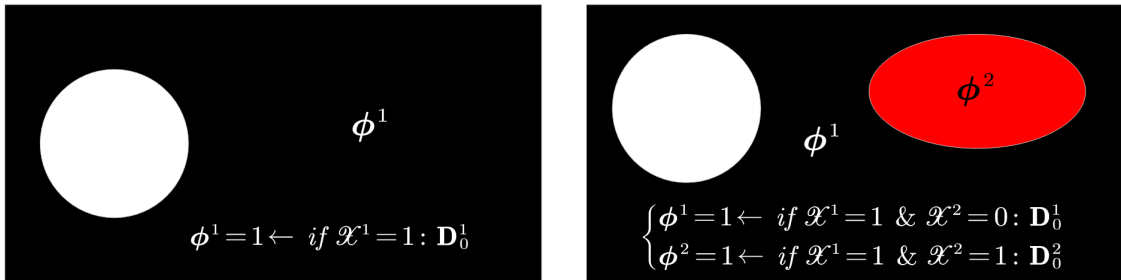
3.2 The Field of Topology Variables (TVF)

As already pointed out in Section 3, we need to introduce the DVFs with a number θ to describe the TVFs, and each TVF is expressed by a function of all DVFs \mathcal{X}^ϑ ($\vartheta = 1, 2, \dots, \theta$), given as:

$$\phi^\vartheta = \prod_{\lambda=1}^{\vartheta} \mathcal{X}^\lambda \prod_{\lambda=\vartheta+1}^{\theta} (1 - \mathcal{X}^\lambda) \quad (11)$$

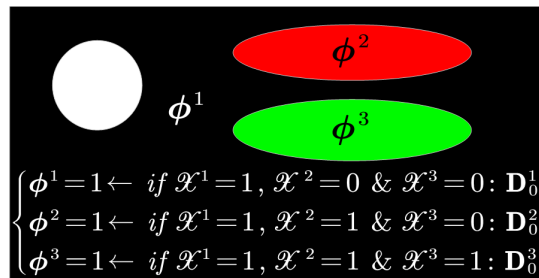
If $\theta = 1, 2, 3$, the detailed forms of the TVFs with respect to DVFs are expressed as:

$$\begin{cases} \theta = 1: & \phi^1 = \mathcal{X}^1 \\ \theta = 2: & \phi^1 = \mathcal{X}^1(1 - \mathcal{X}^2); \phi^2 = \mathcal{X}^1\mathcal{X}^2 \\ \theta = 3: & \phi^1 = \mathcal{X}^1(1 - \mathcal{X}^2)(1 - \mathcal{X}^3); \phi^2 = \mathcal{X}^1\mathcal{X}^2(1 - \mathcal{X}^3); \phi^3 = \mathcal{X}^1\mathcal{X}^2\mathcal{X}^3 \end{cases} \quad (12)$$



(a) One material (two phases)

(b) Two materials (three phases)



(c) Three materials (four phases)

Fig. 4. Multi-material topology description in the N-MMI model

A brief representation is shown in **Fig. 4**, in which θ TVFs are applied to describe the overall layouts of θ distinct materials ($\theta + 1$ phases, including void) in the design domain. Each unique material plotted with a distinct color is presented by one TVF, namely material 1 with the black, material 2 with the red and material 3 with the green. Each TVF for the unique material is related to all DVFs, and we only need to change the value of a DVF every time to display the variation of the phase.

3.3 Multi-material interpolation

As already pointed out in [48,49], the densities at Gauss quadrature points are penalized with a parameter to form a power function, and then interpolated with constitutive elastic tensor to compute the IGA element stiffness matrix. In the current construction of the TVFs for all materials, the TVFs with the densities at any points in the design domain are iteratively evolved during the optimization. Based on material interpolation schemes [4], the Multi-Material Interpolation is expressed by a summation of all the interpolated functions of TVFs with the corresponding physical properties of materials, given by:

$$\mathbf{D} = \sum_{\vartheta=1}^{\theta} \frac{(\phi^{\vartheta})^p}{w_{\vartheta}} \mathbf{D}_0^{\vartheta} = \sum_{\vartheta=1}^{\theta} \underbrace{\left(\prod_{\lambda=1}^{\vartheta} (x^{\lambda}) \prod_{\lambda=\vartheta+1}^{\theta} (1 - x^{\lambda}) \right)^p}_{w_{\vartheta}} \mathbf{D}_0^{\vartheta} \quad (13)$$

where \mathbf{D}_0^{ϑ} is the constitutive elastic property of the ϑ_{th} distinct material, and p is the penalty parameter. As already pointed out in the Introduction, The earlier works have developed many different multi-material interpolation, like the mixture rule [19,20] and the DMO scheme [23] with an extensive discussion. Later, Gao and Zhang [24] divided the DMO scheme into two branches, namely the RMMI and UMMI (UMMI-1 and UMMI-2) models. Here, we present the details of the RMMI, UMMI-1 and UMMI-2 models to show the specific features of the N-MMI model, given in **Table 1**. Meanwhile, as far as three distinct materials, the corresponding formulas using four different multi-material interpolation models are listed in **Table 2**. It is noted that the symbol x denotes variables in the RMMI, UMMI-1 and UMMI-2 models.

The specific features and functions of the RMMI, UMMI-1 and UMMI-2 models can refer to [23,24]. In the authors' viewpoint, the similar feature of them is that both design variables and topology variables are coupled in a unified mathematical symbol, namely x . In the optimization, design variables and topology variables will be advanced in a parallel mechanism, presented in **Fig. 5 (a)**. As already given in [23,24,34], several numerical troubles are occurred in the final designs, such as the unrealistic designs with the "mixed" materials, the local solution and etc. The main reason originates from the inseparability of design variables and topology variables, as well as the high nonlinearity of sensitivity analysis with variables.

Table 1. The formulas of three multi-material interpolation models

Models	Formulas
RMMI	$\mathbf{D} = \sum_{\vartheta=1}^{\vartheta} (x^0)^p \underbrace{\left(\prod_{\lambda=1}^{\vartheta-1} [1 - (x^{\vartheta \neq \lambda})^p] (x^\lambda)^p \right)}_{\tilde{w}_\vartheta} \mathbf{D}_0^\vartheta$
UMMI-1	$\mathbf{D} = \sum_{\vartheta=1}^{\vartheta} \underbrace{(x^\vartheta)^p}_{\tilde{w}_\vartheta} \mathbf{D}_0^\vartheta$
UMMI-2	$\mathbf{D} = \sum_{\vartheta=1}^{\vartheta} (x^\vartheta)^p \underbrace{\prod_{\lambda=1}^{\vartheta} [1 - (x^{\lambda \neq \vartheta})^p]}_{\tilde{w}_\vartheta} \mathbf{D}_0^\vartheta$

Table 2. The formulas of three distinct materials using different models

Models	Three distinct materials
RMMI	$\mathbf{D} = \underbrace{(x^0)^p [1 - (x^1)^p]}_{\tilde{w}_1} \mathbf{D}_0^1 + \underbrace{(x^0)^p (x^1)^p [1 - (x^2)^p]}_{\tilde{w}_2} \mathbf{D}_0^2 + \underbrace{(x^0)^p (x^1)^p (x^2)^p}_{\tilde{w}_3} \mathbf{D}_0^3$
UMMI-1	$\mathbf{D} = \underbrace{(x^1)^p}_{\tilde{w}_1} \mathbf{D}_0^1 + \underbrace{(x^2)^p}_{\tilde{w}_2} \mathbf{D}_0^2 + \underbrace{(x^3)^p}_{\tilde{w}_3} \mathbf{D}_0^3$
UMMI-2	$\mathbf{D} = \underbrace{(x^1)^p (1 - (x^2)^p) (1 - (x^3)^p)}_{\tilde{w}_1} \mathbf{D}_0^1 + \underbrace{(x^2)^p [1 - (x^1)^p] [1 - (x^3)^p]}_{\tilde{w}_2} \mathbf{D}_0^2 + \underbrace{(x^3)^p [1 - (x^1)^p] [1 - (x^2)^p]}_{\tilde{w}_3} \mathbf{D}_0^3$
N-MMI	$\mathbf{D} = \underbrace{[\mathcal{X}^1 (1 - \mathcal{X}^2) (1 - \mathcal{X}^3)]^p}_{\tilde{w}_1} \mathbf{D}_0^1 + \underbrace{[\mathcal{X}^1 \mathcal{X}^2 (1 - \mathcal{X}^3)]^p}_{\tilde{w}_2} \mathbf{D}_0^2 + \underbrace{[\mathcal{X}^1 \mathcal{X}^2 \mathcal{X}^3]^p}_{\tilde{w}_3} \mathbf{D}_0^3$

Hence, in the current work, the key intention is to develop an improved multi-material interpolation model using NURBS, namely the N-MMI model. The corresponding formula is shown in Eq. (13). We can find that the developed N-MMI can be viewed as a following branch of the initial DMO scheme, but with several improvements. Firstly, design variables and topology variables are decoupled, so that the latter optimization of them will be in a serial mechanism, shown in **Fig. 5 (b)**. This basic feature will offer benefits for omitting some numerical troubles to some extent. Moreover, the separability between design variables and topology variables can be beneficial to lower the complexity degree of sensitivity analysis with respect to variables, and sensitivity analysis of the constraint functions is linear with respect to the topology variables. Hence, in the viewpoint of topology variables, the formula of the N-MMI is same as the UMMI-1 model, which is also analogous to the UMMI-2 model considering design variables. Overall speaking, the current N-MMI model has the following advantages: (1) All TVFs with the sufficient smoothness and continuity are applied to display the layouts of multiple materials, rather than a discrete form with a series of element densities; (2) Each TVF can exactly present the distribution of a unique material; (3) The combination of all DVFs

for the expression of the TVF can ensure no overlaps between multiple materials and no redundant phases in the design domain, and there is no need to introduce additional constraints for variables; (4) The explicit mathematical formula offers more benefits for the latter sensitivity analysis in the formulation.

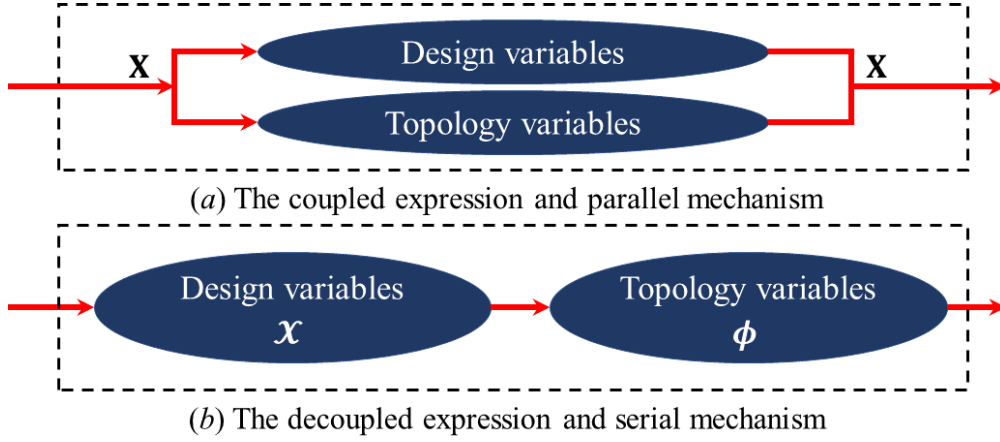


Fig. 5. The expression and evolving mechanisms of design variables and topology variables

4 Multi-material Isogeometric topology optimization (M-ITO)

4.1 M-ITO formulation to minimize the structural mean compliance

The minimization of the structural mean compliance for linearly elastic structures will be studied to present the effectiveness of the proposed N-MMI model, and the M-ITO formulation for the problem with multiple volume constraints can be stated as:

$$\begin{cases} \text{Find: } \rho_{i,j}^{\vartheta} & (\vartheta = 1, 2, \dots, \Theta; i = 1, 2, \dots, n; j = 1, 2, \dots, m) \\ \text{Min: } J(\mathbf{u}, \boldsymbol{\phi}) = \frac{1}{2} \int_{\Omega} \mathbf{D}(\boldsymbol{\phi}(\rho_{i,j}^{\vartheta})) \boldsymbol{\varepsilon}(\mathbf{u}) \boldsymbol{\varepsilon}(\mathbf{u}) d\Omega \\ \text{s. t: } \begin{cases} a(\mathbf{u}, \delta \mathbf{u}) = l(\delta \mathbf{u}), \mathbf{u}|_{\Gamma_D} = \mathbf{g}, \forall \delta \mathbf{u} \in H^1(\Omega) \\ G_v^{\hat{\vartheta}} = \frac{1}{|\Omega|} \int_{\Omega} \phi^{\hat{\vartheta}}(\rho_{i,j}^{\vartheta}) v_0 d\Omega - V_0^{\hat{\vartheta}} \leq 0, \quad (\hat{\vartheta} = 1, 2, \dots, \Theta) \\ 0 \leq \rho_{i,j}^{\vartheta} \leq 1, \quad \boldsymbol{\phi} = \{\phi^{\vartheta}\}, (\vartheta = 1, 2, \dots, \Theta) \end{cases} \end{cases} \quad (14)$$

where $\rho_{i,j}^{\vartheta}$ is the $(i,j)_{th}$ control design variable for the ϑ_{th} DVF. J is the objective function defined by the structural mean compliance. $G_v^{\hat{\vartheta}}$ is the volume constraint for the $\hat{\vartheta}_{th}$ unique material, and $V_0^{\hat{\vartheta}}$ is its maximum material consumption, and v_0 is the volume fraction of the solid. We can find that all the volume constraints have the separable and linear form with respect to the corresponding TVF $\phi^{\hat{\vartheta}}$. $\phi^{\hat{\vartheta}}$ is the $\hat{\vartheta}_{th}$ TVF to represent the layout of the $\hat{\vartheta}_{th}$ unique material. \mathbf{u} is the displacement field in the domain Ω , and \mathbf{g} is the prescribed displacement vector on Γ_D , and $\delta \mathbf{u}$ is the virtual displacement field belonging to the space $H^1(\Omega)$. a and l are the bilinear energy and linear load functions, given as:

$$\begin{cases} a(\mathbf{u}, \delta \mathbf{u}) = \int_{\Omega} \mathbf{D}(\boldsymbol{\phi}(\rho_{i,j}^{\vartheta})) \boldsymbol{\varepsilon}(\mathbf{u}) \boldsymbol{\varepsilon}(\delta \mathbf{u}) d\Omega \\ l(\delta \mathbf{u}) = \int_{\Omega} \mathbf{f} \delta \mathbf{u} d\Omega + \int_{\Gamma_N} \mathbf{h} \delta \mathbf{u} d\Gamma_N \end{cases} \quad (15)$$

where \mathbf{f} is the body force and \mathbf{h} is the boundary traction on Γ_N . In order to demonstrate the ability of the proposed M-ITO method to seek the optimum, a more practical problem with the total mass constraint is studied, and the alternative formulation is written as:

$$\begin{cases} \text{Find: } \rho_{i,j}^{\vartheta} \quad (\vartheta = 1, 2, \dots, \theta; i = 1, 2, \dots, n; j = 1, 2, \dots, m) \\ \text{Min: } J(\mathbf{u}, \boldsymbol{\phi}) = \frac{1}{2} \int_{\Omega} \mathbf{D}(\boldsymbol{\phi}(\rho_{i,j}^{\vartheta})) \boldsymbol{\varepsilon}(\mathbf{u}) \boldsymbol{\varepsilon}(\mathbf{u}) d\Omega \\ \text{S. t: } \begin{cases} a(\mathbf{u}, \delta \mathbf{u}) = l(\delta \mathbf{u}), \mathbf{u}|_{\Gamma_D} = \mathbf{g}, \forall \delta \mathbf{u} \in H^1(\Omega) \\ G_m = \sum_{\hat{\vartheta}=1}^{\theta} G_v^{\hat{\vartheta}} \Lambda_0^{\hat{\vartheta}} - M_0 \leq 0, \quad (\hat{\vartheta} = 1, 2, \dots, \theta) \\ 0 \leq \rho_{i,j}^{\vartheta} \leq 1, \quad \boldsymbol{\phi} = \{\phi^{\vartheta}\}, (\vartheta = 1, 2, \dots, \theta) \end{cases} \end{cases} \quad (16)$$

where $\Lambda_0^{\hat{\vartheta}}$ is the mass density of the $\hat{\vartheta}_{th}$ unique material, and M_0 is the maximal value of the structural mass in the constraint G_m . As we can see, the formulation 2 in Eq. (16) can simultaneously consider the influence of volume fractions and the structural mass on the selection of materials in the optimization. The total mass constraint is also featured with a separable-linear form of the TVF $\phi^{\hat{\vartheta}}$. This positive feature can lower the numerical troubles in the optimization to a great extent. It should be noticed that the formulation with multiple mass constraints are physically equivalent to the formulation 1 in Eq. (15), due to a fact that the volume constraint for each distinct material is separable and linear with respect to the TVF $\phi^{\hat{\vartheta}}$ of the $\hat{\vartheta}_{th}$ material. Multiple volume constraints can be directly converted into mass constraints by multiplying the corresponding mass density on both sides.

4.2 Sensitivity analysis of the objective function

In Eqs. (14) and (16), the objective function is defined by the structural mean compliance. The first-order derivative of the structural mean compliance with respect to the TVF $\phi^{\hat{\vartheta}}$ can be derived as:

$$\frac{\partial J}{\partial \phi^{\hat{\vartheta}}} = \int_{\Omega} \mathbf{D}(\boldsymbol{\phi}) \boldsymbol{\varepsilon}(\dot{\mathbf{u}}) \boldsymbol{\varepsilon}(\mathbf{u}) d\Omega + \frac{1}{2} \int_{\Omega} \frac{\partial \mathbf{D}(\boldsymbol{\phi})}{\partial \phi^{\hat{\vartheta}}} \boldsymbol{\varepsilon}(\mathbf{u}) \boldsymbol{\varepsilon}(\mathbf{u}) d\Omega, \quad (\hat{\vartheta} = 1, 2, \dots, \theta) \quad (17)$$

where $\dot{\mathbf{u}}$ is the first-order derivative of the displacement field with respect to the TVF $\phi^{\hat{\vartheta}}$. According to the derivations in [48,49], we can obtain the following equation, given as:

$$\int_{\Omega} \mathbf{D}(\boldsymbol{\phi}) \boldsymbol{\varepsilon}(\dot{\mathbf{u}}) \boldsymbol{\varepsilon}(\mathbf{u}) d\Omega = - \int_{\Omega} \frac{\partial \mathbf{D}(\boldsymbol{\phi})}{\partial \phi^{\hat{\vartheta}}} \boldsymbol{\varepsilon}(\mathbf{u}) \boldsymbol{\varepsilon}(\mathbf{u}) d\Omega \quad (18)$$

Substituting Eq. (18) into Eq. (17). The first-order derivative of the structural mean compliance with respect to the TVF $\phi^{\hat{\vartheta}}$ is obtained, explicitly expressed as:

$$\frac{\partial J}{\partial \phi^{\hat{\vartheta}}} = -\frac{1}{2} \int_{\Omega} \frac{\partial \mathbf{D}(\boldsymbol{\phi})}{\partial \phi^{\hat{\vartheta}}} \boldsymbol{\varepsilon}(\mathbf{u}) \boldsymbol{\varepsilon}(\mathbf{u}) d\Omega, \quad (\hat{\vartheta} = 1, 2, \dots, \theta) \quad (19)$$

Hence, the sensitivity of the objective function can be achieved by calculating the first-order derivative of the elastic tensor with respect to the TVF $\phi^{\hat{\vartheta}}$. According to the N-MMI model, the sensitivity analysis of the multi-material elastic tensor can be directly obtained, and a new form of Eq. (19) is given as:

$$\frac{\partial J}{\partial \phi^{\hat{\vartheta}}} = -\frac{1}{2} \int_{\Omega} p(\phi^{\hat{\vartheta}})^{p-1} \mathbf{D}_0^{\hat{\vartheta}} \boldsymbol{\varepsilon}(\mathbf{u}) \boldsymbol{\varepsilon}(\mathbf{u}) d\Omega \quad (20)$$

In Section 3.2, the TVF $\phi^{\hat{\vartheta}}$ to display the layout of the $\hat{\vartheta}$ unique material is expressed as a combination of all DVFs, and each DVF is developed by NURBS basis functions with control design variables $\boldsymbol{\rho}^{\vartheta}$. we can firstly derive the derivative of the TVF $\phi^{\hat{\vartheta}}$ with respect to the DVF \mathcal{X}^{ϑ} , given as:

$$\frac{\partial \phi^{\hat{\vartheta}}}{\partial \mathcal{X}^{\vartheta}} = \begin{cases} \prod_{\lambda=1, \lambda \neq \vartheta}^{\hat{\vartheta}} \mathcal{X}^{\lambda} \prod_{\lambda=\hat{\vartheta}+1}^{\theta} (1 - \mathcal{X}^{\lambda}) & \text{if } \vartheta \leq \hat{\vartheta} \\ -\prod_{\lambda=1}^{\hat{\vartheta}} \mathcal{X}^{\lambda} \prod_{\lambda=\hat{\vartheta}+1, \lambda \neq \vartheta}^{\theta} (1 - \mathcal{X}^{\lambda}) & \text{if } \vartheta > \hat{\vartheta} \end{cases} \quad (\vartheta = 1, 2, \dots, \theta) \quad (21)$$

Then, the derivative of the DVF with respect to control design variables can be derived by:

$$\frac{\partial \mathcal{X}^{\vartheta}}{\partial \rho_{i,j}^{\vartheta}} = \frac{\partial \mathcal{X}^{\vartheta}}{\partial \mathcal{G}^{\vartheta}} \frac{\partial \mathcal{G}^{\vartheta}}{\partial \rho_{i,j}^{\vartheta}} = R_{i,j}^{p,q}(\xi, \eta) \psi(\rho_{i,j}^{\vartheta}) \quad (22)$$

where $R_{i,j}^{p,q}(\xi, \eta)$ is the NURBS basis function at the computational point (ξ, η) . $\psi(\rho_{i,j}^{\vartheta})$ is the Shepard function at the control point (i, j) . It is important to notice that the computational point (ξ, η) is different from the control point (i, j) . In the formulation 1 and 2, the computational points correspond to the Gauss quadrature points. Hence, the derivative of the structural mean compliance with respect to the control design variables can be derived by Eqs. (20)-(22), and expressed as:

$$\frac{\partial J}{\partial \rho_{i,j}^\vartheta} = \frac{\partial J}{\partial \boldsymbol{\phi}} \frac{\partial \boldsymbol{\phi}}{\partial \mathcal{X}^\vartheta} \frac{\partial \mathcal{X}^\vartheta}{\partial \rho_{i,j}^\vartheta} = \sum_{\hat{\vartheta}=1}^{\vartheta} \frac{\partial J}{\partial \boldsymbol{\phi}^{\hat{\vartheta}}} \frac{\partial \boldsymbol{\phi}^{\hat{\vartheta}}}{\partial \mathcal{X}^\vartheta} \frac{\partial \mathcal{X}^\vartheta}{\partial \rho_{i,j}^\vartheta} =$$

$$\sum_{\hat{\vartheta}=1}^{\vartheta} \left\{ \begin{array}{l} \left\{ -\frac{1}{2} \int_{\Omega} \left(p(\mathcal{X}^\vartheta)^{p-1} \left(\prod_{\lambda=1, \lambda \neq \vartheta}^{\hat{\vartheta}} \mathcal{X}^\lambda \prod_{\lambda=\hat{\vartheta}+1}^{\vartheta} (1-\mathcal{X}^\lambda) \right)^p \right) \mathbf{D}_0^{\hat{\vartheta}} \dots \right. \\ \left. R_{i,j}^{p,q}(\xi, \eta) \psi(\rho_{i,j}^\vartheta) \boldsymbol{\varepsilon}(\mathbf{u}) \boldsymbol{\varepsilon}(\mathbf{u}) d\Omega \right\} \quad \text{if } \vartheta \leq \hat{\vartheta} \\ \left\{ -\frac{1}{2} \int_{\Omega} \left(-p(1-\mathcal{X}^\vartheta)^{p-1} \left(\prod_{\lambda=1}^{\hat{\vartheta}} \mathcal{X}^\lambda \prod_{\lambda=\hat{\vartheta}+1, \lambda \neq \vartheta}^{\vartheta} (1-\mathcal{X}^\lambda) \right)^p \right) \mathbf{D}_0^{\hat{\vartheta}} \dots \right. \\ \left. R_{i,j}^{p,q}(\xi, \eta) \psi(\rho_{i,j}^\vartheta) \boldsymbol{\varepsilon}(\mathbf{u}) \boldsymbol{\varepsilon}(\mathbf{u}) d\Omega \right\} \quad \text{if } \vartheta > \hat{\vartheta} \end{array} \right\} \quad (23)$$

In Eq. (23), we can see that the sensitivity analysis of the objective function with respect to control design variables consist of the DVFs, elastic tensors, NURBS basis functions and Shepard function. The NURBS basis functions used in IGA keep unchanged, and the Shepard function only depends on the spatial locations of control points. They can be pre-stored without using the additional storage space, so that the sensitivity analysis is also cost-effective.

4.3 Sensitivity analysis of constraint functions

In formulations 1 and 2, two different constraints are defined, containing multiple volume fractions and the total mass constraint. As far as multiple volume constraints, the derivatives of all volume constraints with respect to control design variables can be derived, as:

$$\frac{\partial G_v^{\hat{\vartheta}}}{\partial \rho_{i,j}^\vartheta} = \frac{\partial G_v^{\hat{\vartheta}}}{\partial \boldsymbol{\phi}^{\hat{\vartheta}}} \frac{\partial \boldsymbol{\phi}^{\hat{\vartheta}}}{\partial \mathcal{X}^\vartheta} \frac{\partial \mathcal{X}^\vartheta}{\partial \rho_{i,j}^\vartheta} =$$

$$\left\{ \begin{array}{l} \frac{1}{|\Omega|} \int_{\Omega} \left(\left(\prod_{\lambda=1, \lambda \neq \vartheta}^{\hat{\vartheta}} \mathcal{X}^\lambda \prod_{\lambda=\hat{\vartheta}+1}^{\vartheta} (1-\mathcal{X}^\lambda) \right) R_{i,j}^{p,q}(\xi, \eta) \psi(\rho_{i,j}^\vartheta) \right) v_0 d\Omega \quad \text{if } \vartheta \leq \hat{\vartheta} \\ -\frac{1}{|\Omega|} \int_{\Omega} \left(\left(\prod_{\lambda=1}^{\hat{\vartheta}} \mathcal{X}^\lambda \prod_{\lambda=\hat{\vartheta}+1, \lambda \neq \vartheta}^{\vartheta} (1-\mathcal{X}^\lambda) \right) R_{i,j}^{p,q}(\xi, \eta) \psi(\rho_{i,j}^\vartheta) \right) v_0 d\Omega \quad \text{if } \vartheta > \hat{\vartheta} \end{array} \right\} \quad (24)$$

The first-order derivative of the total mass constraint in formulation 2 can be derived by the summation of all derivatives of multiple volume constraints with mass densities in Eq. (24), expressed as:

$$\frac{\partial G_m}{\partial \rho_{i,j}^\vartheta} = \sum_{\hat{\vartheta}=1}^{\theta} \frac{\partial G_v^{\hat{\vartheta}}}{\partial \rho_{i,j}^\vartheta} \Lambda_0^{\hat{\vartheta}} = \sum_{\hat{\vartheta}=1}^{\theta} \left\{ \begin{array}{l} \frac{1}{|\Omega|} \int_{\Omega} \left(\left(\prod_{\lambda=1, \lambda \neq \vartheta}^{\hat{\vartheta}} \mathcal{X}^\lambda \prod_{\lambda=\hat{\vartheta}+1}^{\theta} (1 - \mathcal{X}^\lambda) \right) R_{i,j}^{p,q}(\xi, \eta) \psi(\rho_{i,j}^\vartheta) \right) \Lambda_0^{\hat{\vartheta}} v_0 d\Omega \quad \text{if } \vartheta \leq \hat{\vartheta} \\ -\frac{1}{|\Omega|} \int_{\Omega} \left(\left(\prod_{\lambda=1}^{\hat{\vartheta}} \mathcal{X}^\lambda \prod_{\lambda=\hat{\vartheta}+1, \lambda \neq \vartheta}^{\theta} (1 - \mathcal{X}^\lambda) \right) R_{i,j}^{p,q}(\xi, \eta) \psi(\rho_{i,j}^\vartheta) \right) \Lambda_0^{\hat{\vartheta}} v_0 d\Omega \quad \text{if } \vartheta > \hat{\vartheta} \end{array} \right. \quad (25)$$

Hereto, the sensitivity analysis for two formulations, including the objective and constraint functions, are derived in detail from Eqs. (17) to (25). Recently, several optimization algorithms have been proposed to solve the related problems [3,58–60]. The method of moving asymptotes (MMA) [60] is applied to evolve control design variables in the next numerical examples.

5. Numerical Examples

In this section, several numerical examples are performed to demonstrate the effectiveness of the proposed M-ITO method. All structures with the linear elasticity are considered, and 2D structures will be discretized with the IGA elements with unit edge thickness. In all examples, the magnitude of the loaded force is equal to unit, and 3 × 3 (2D) or 3 × 3 × 3 (3D) Gauss quadrature points are chosen to solve the IGA element stiffness matrix. The initial values of all control design variables ρ^ϑ ($\vartheta = 1, 2, \dots, \theta$) are defined as 0.5, and the penalty factor p is set to be 3, which keeps consistent with the interpolation model for the single material [1,4]. The optimization will be terminated if the maximum change of the DVFs is lower than 1% in 300 iterations. Four “virtual” isotropic solid materials will be considered in next examples, and the details are provided in **Table 3**, including the Young’s modulus, Poisson’s ratio, Mass density and the stiffness-to-mass ratio.

Table 3. Four “virtual” isotropic solid materials

i	Materials	Young’s modulus: E_0^i	Poisson’s ratio ν	Mass density: Λ_0^i	Stiffness-to-mass ratio: \mathcal{R}_0^i
1	M1	10	0.3	2	5
2	M2	10	0.3	5	2
3	M3	5	0.3	2	2.5
4	M4	3	0.3	2	1.5

5.1 Messerschmitt-Bolkow-Blohm (MBB) beam

The formulation 1 with multiple volume constraints is applied to optimize the MBB beam in this example. In **Fig. 6**, the MBB beam with the loads and boundary conditions is defined, and two indices L and H are

set as 18 and 3, respectively. The NURBS is applied to parameterize the MBB beam. The details are listed below **Fig. 6**, where the quadratic NURBS basis functions are used.

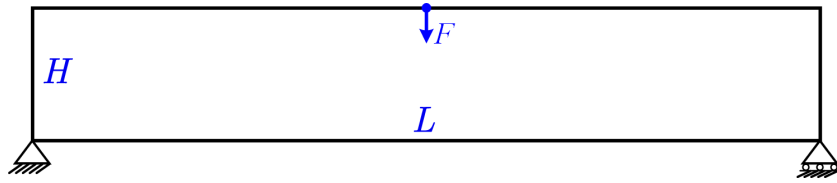


Fig. 6. MBB beam: IGA elements 180×30 ; $\Xi = \{0,0,0,0.00565, \dots, 0.99444, 1,1,1\}$, $\mathcal{H} = \{0,0,0,0.0333, \dots, 0.9667, 1,1,1\}$; $n = 182, m = 32$; $p = q = 2$.

5.1.1 Two-material design

In this case, two distinct materials (**M2** and **M3**) are available in the optimization of the MBB beam. Two TVFs need to be defined for **M2** and **M3** materials, respectively, denoted by ϕ^1 and ϕ^2 . In Eq. (14), the allowable material volume fractions for **M2** and **M3** are defined as 20% and 8%, respectively. As discussed in Sections 3 and 4.3, the Gauss quadrature points work as the computational ones to compute the stiffness matrix. In numerical results, we firstly show the TVFs at Gauss quadrature points (GQPs) and then display the TVFs in the design domain. As given in Section 3.1, the DVF corresponds to a NURBS surface with the strict physical meanings (densities) for the design domain, and each TVF is a combination of all DVFs. Hence, a TVF can be regarded as a density distribution function to represent the distribution of each distinct material in the design domain. The initial values of control design variables are 0.5, and the corresponding initial designs of the TVFs for two materials are shown in **Fig. 7**, including the TVFs at GQPs and in the design domain. It can be found that the TVFs at GQPs denote the discretized distribution of densities, and the TVFs in the design domain denote the continuous form of the density distribution.

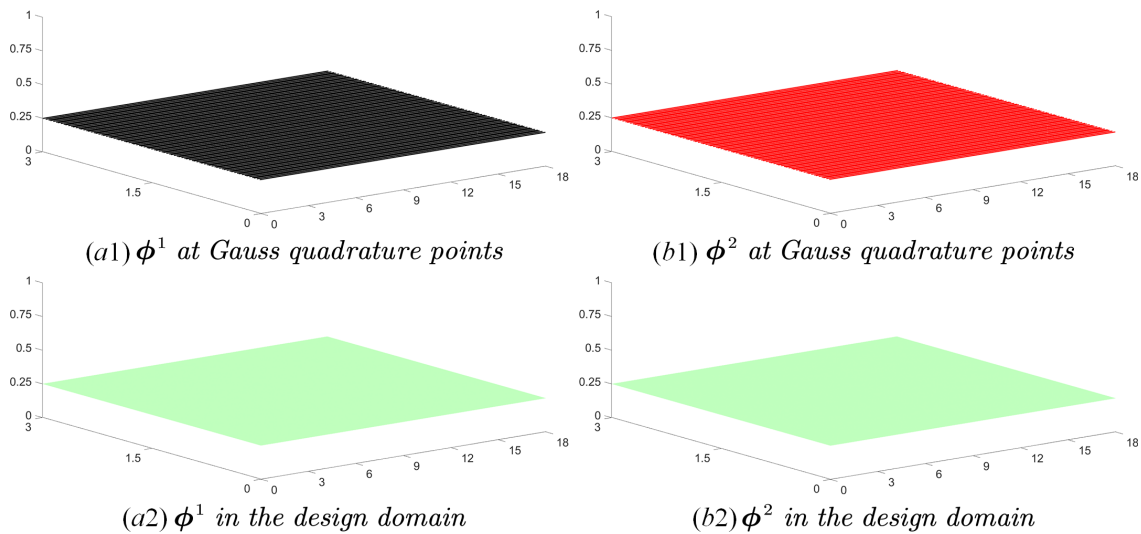


Fig. 7. Initial design of the MBB beam

As displayed in **Fig. 8**, the optimized design of the MBB beam with two distinct materials (**M2** and **M3**) is provided, including the TVFs at GQPs and also in the design domain. As we can see, the TVFs are featured with the sufficient smoothness and continuity, resulting from the construction of DVFs using NURBS basis functions and the Shepard function. The former can make sure the continuity, and the latter guarantees the smoothness. Moreover, it can easily be seen that the densities of the optimized TVFs in the design domain are mostly distributed nearly the lower and upper bounds.

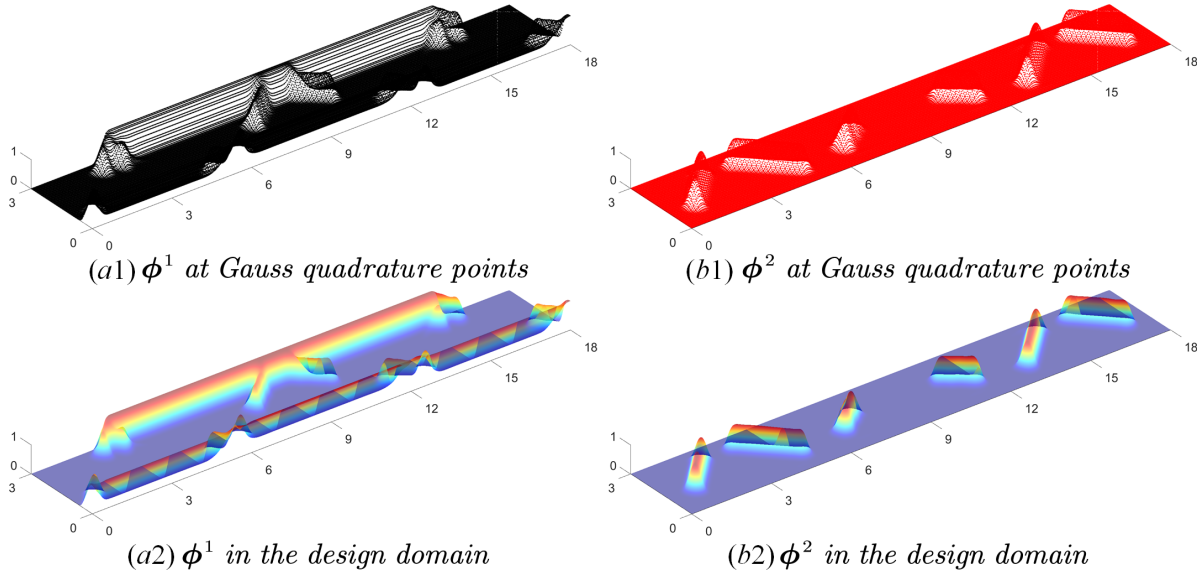


Fig. 8. The optimized design of the MBB beam

Based on the optimized design of the MBB beam displayed in **Fig. 8**, a simple but efficient heuristic scheme is introduced to define the structural topology, and the corresponding mathematical model is defined in Eq. (26), where ϕ_c is a constant. As we can see, the structural boundary of the MBB beam is expressed by the iso-contour of ϕ . ϕ with the values higher than ϕ_c represents the solids in the design domain, and the values lower than ϕ_c describes voids. Hence, this scheme is very analogous to the implicit representation model in the LSM [6–8]. However, it is important to note that the heuristic scheme is just a post-definition criterion to obtain the structural topology from the optimized TVFs.




$$\begin{cases} 0 \leq \phi(\xi, \eta) < \phi_c & \text{void} \\ \phi(\xi, \eta) = \phi_c & \text{boundary} \\ \phi_c < \phi(\xi, \eta) \leq 1 & \text{solid} \end{cases} \quad (26)$$

As discussed in [48,49] for the optimization of the single-material problems, the constant equal to 0.5 can ensure that the final volume fraction of the obtained topology is mostly identical to the prescribed allowable volume fraction. In [48], the extensive discussions about the definition of the constant are performed. Here, the post-definition scheme is applied to define the topology for the multi-material problems from the TVFs. The constant should be equal to 0.5 to guarantee no overlaps between different materials and no redundant

phases in the N-MMI model. For example, if the constant ϕ_c is equal to 0.2, it means that the densities at the structural boundaries of **M2** and **M3** materials are both equal to 0.2, and the summation of them is equal to 0.4, which cannot satisfy the summation of the densities of all materials in each designable point is equal to 1. Hence, the constant ϕ_c must be equal to 0.5 to guarantee the reasonable physical meanings of the N-MMI model. As listed in **Table 4**, the optimized results of the MBB beam with two materials are provided, including the 2D-view of the TVF ϕ^1 with higher values than ϕ_c at GQPs, the topology of **M2** material, the 2D-view of the TVF ϕ^2 with higher values than ϕ_c at GQPs, the topology of **M3** material, the TVFs ϕ^1 and ϕ^2 at GQPs and in the design domain, the 2D-view of the TVFs ϕ^1 and ϕ^2 at GQPs, and the topology of two materials. The volume fraction of the topology of **M2** material is equal to 19.8% (nearly 20%), and the volume fraction of the topology of **M3** material is equal to 7.9% (nearly 8%). Hence, the volume fraction of the topology of two materials in the MBB beam is equal to 27.7% (also nearly 28%).

Additionally, each distinct material in the final two-material design can form the independent load-bearing structural members, as displayed in **Table 4**, due to a fact that the Young’s modulus is comparable between two materials (**M2** with $E_0^2 = 10$ and **M3** with $E_0^3 = 5$), also given in [1,33]. To this end, the optimized design in this example can present the effectiveness of the developed M-ITO method to seek for the layout of multiple materials in the design domain. A pure design, that each point only has one phase, demonstrates the effectiveness of the proposed N-MMI model. Finally, the iterative curves for the objective function and two volume fractions are shown in **Fig. 9**, which displays the stable convergence to arrive at the final design, and the volume fraction of each distinct material can be preserved. It is noted that the volume fractions in the iterative curves correspond to the TVFs ϕ^1 and ϕ^2 for two materials. However, the volume fractions in **Table 4** of the topologies for two materials are defined by the TVFs with a slight modification, namely $\phi \leftarrow 1$ (if $\phi \geq \phi_c$) and $\phi \leftarrow 0$ (if $\phi < \phi_c$).

Table 4. The optimized results of the MBB beam with two materials

M2 material	2D-view of the TVF ϕ^1 at GQPs 	The topology 
	M3 material	2D-view of the TVF ϕ^2 at GQPs 
The TVFs ϕ^1 and ϕ^2 at GQPs		The TVFs ϕ^1 and ϕ^2 in the design domain

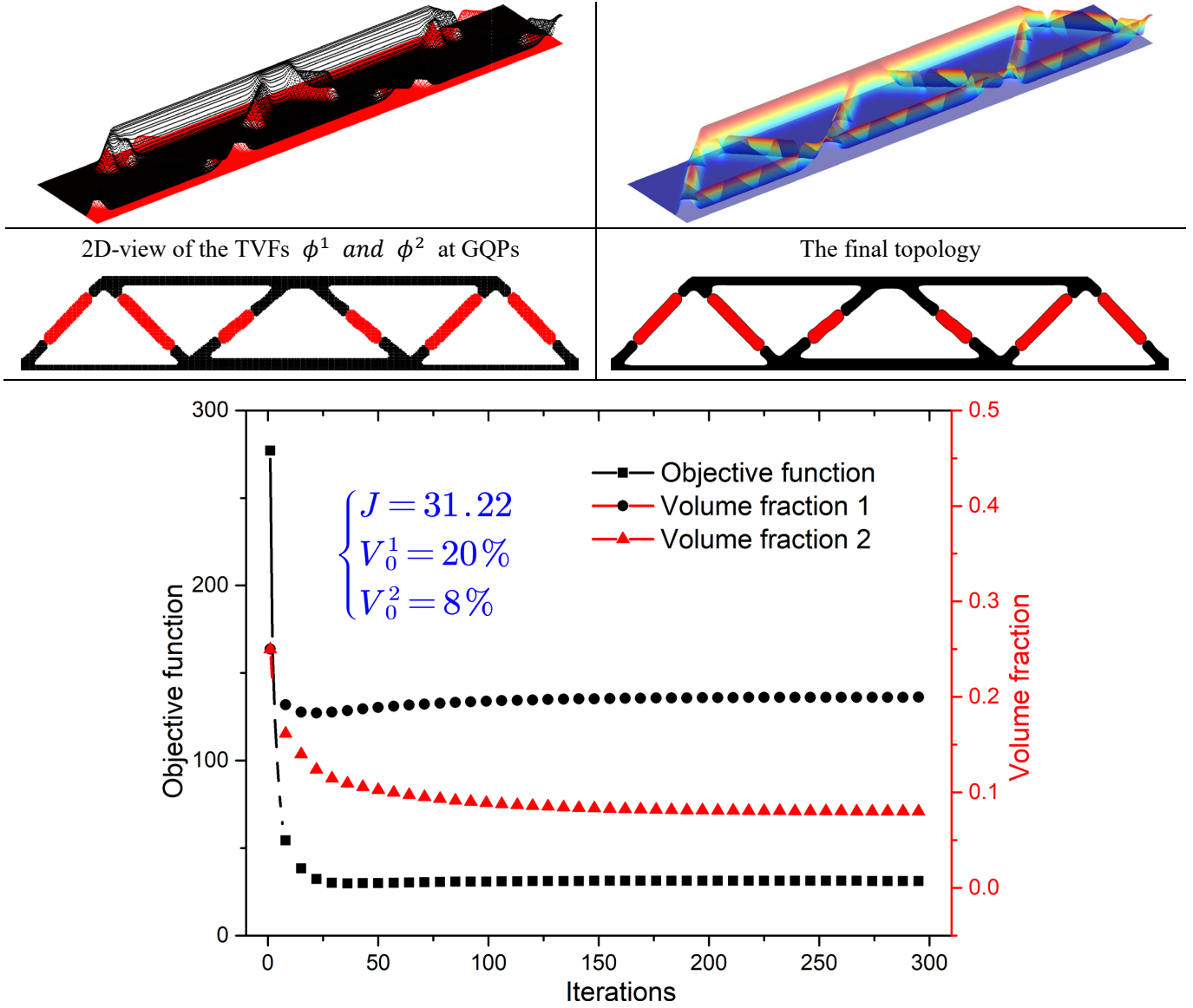


Fig. 9. Convergent histories

5.1.2 Three-material design

This case will consider the three-material topology optimization for the MBB beam, and **M2**, **M3** and **M4** materials will be available, and the corresponding volume fractions for three materials are set as 20%, 12% and 3%, respectively. The initial designs of the TVFs for **M2**, **M3** and **M4** materials are illustrated in **Fig. 10**, including the TVFs at GQPs and in the design domain.

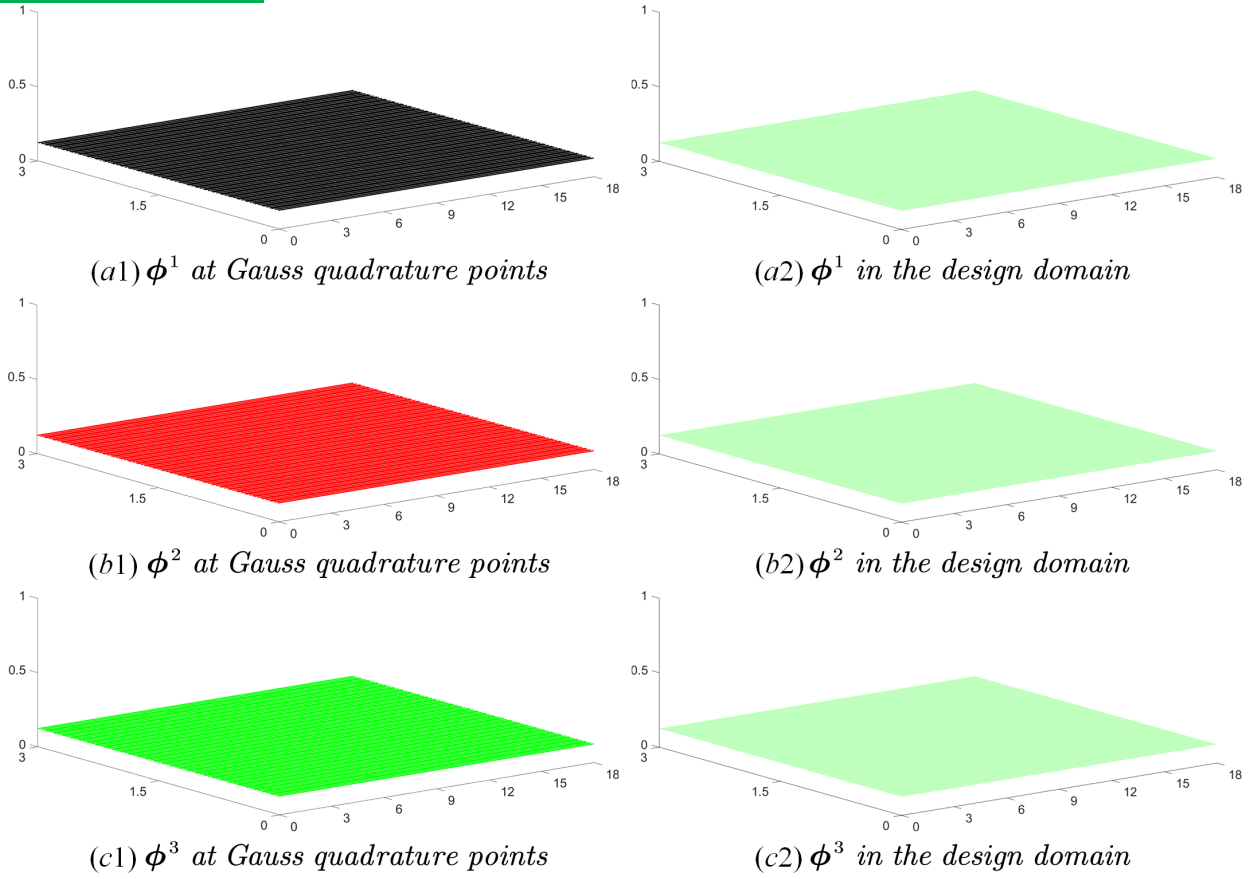


Fig. 10. Initial design of the MBB beam

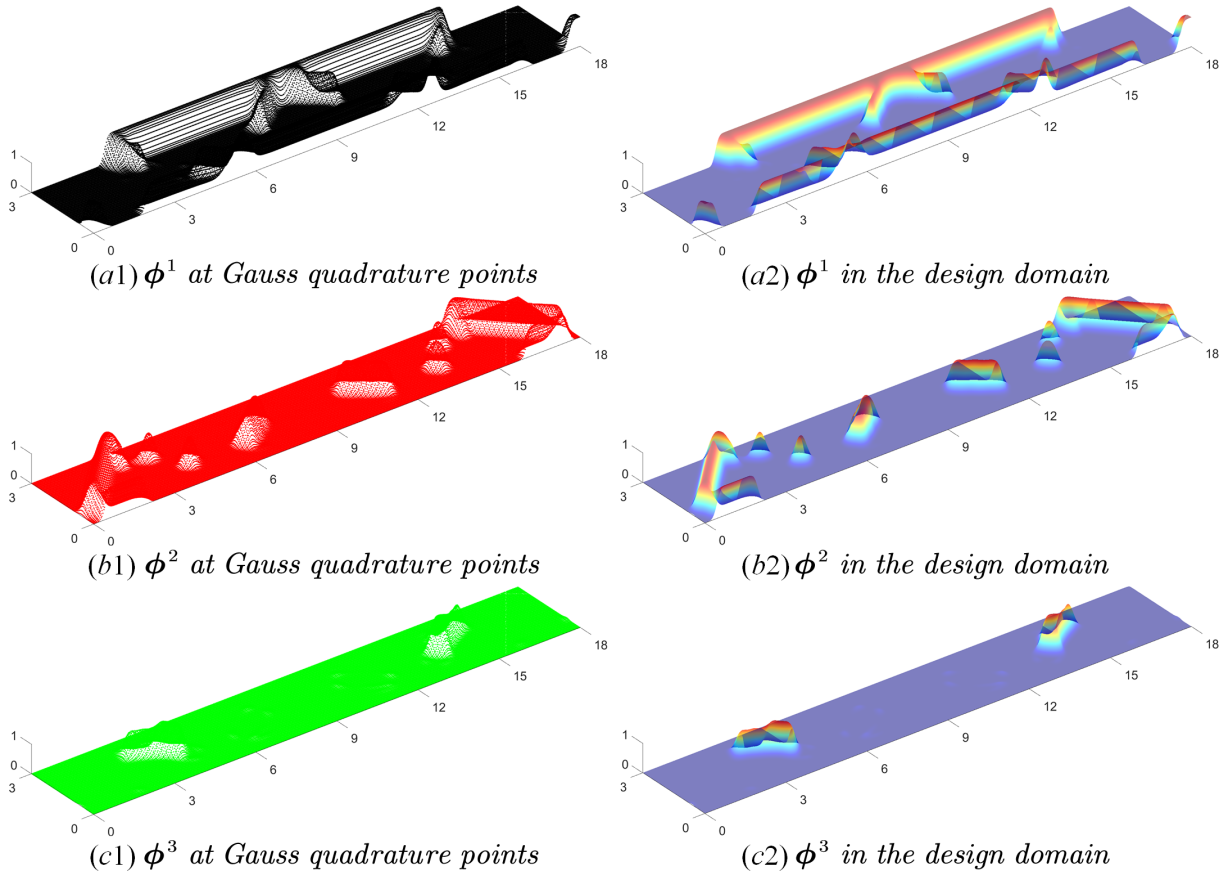


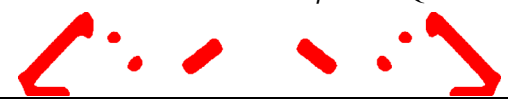
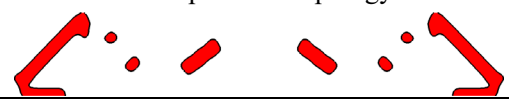
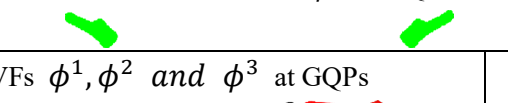
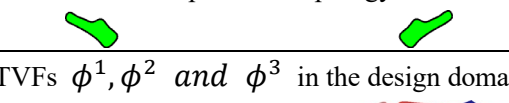
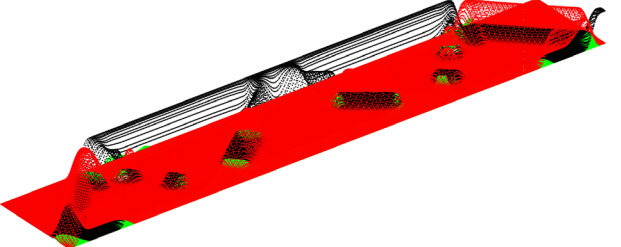
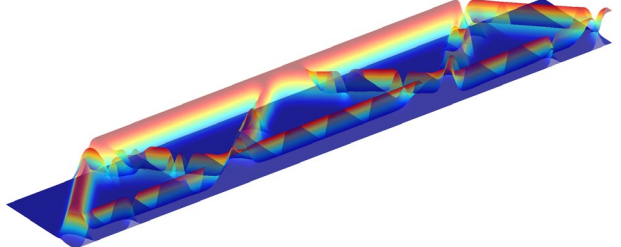
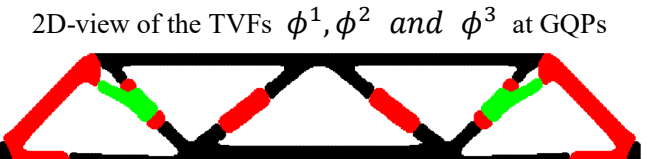
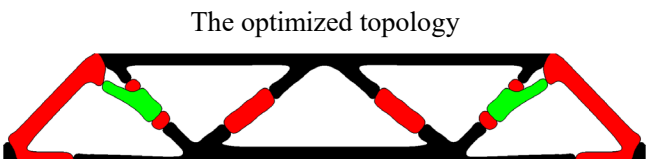


Fig. 11. The optimized design of the MBB beam

The optimized designs of the TVFs for three materials are displayed in **Fig. 11**, consisting of the discretized distributions of the TVFs at GQPs, and the continuous distributions of the TVFs in the design domain. It

can be easily seen that three continuous distributions of the TVFs are featured with the enough continuity and smoothness. The heuristic scheme in Eq. (26) is employed here to define the structural topology of the MBB beam with three materials, shown in Fig. 11, and ϕ_c is still defined as 0.5. The numerical results of three materials in the MBB beam are listed in Table 5, including the 2D-views of the TVFs at GQPs with the values higher than 0.5, and the topologies of three materials in the design domain. We can easily find that the three-material topology of the MBB beam is featured with the distinct interfaces between multiple materials and voids. The necessary requirements discussed in Section 3 can be perfectly maintained in the final three-material topology, such as no overlaps, no redundant phases and so on. Hence, the effectiveness of the proposed N-MMI model in the optimization can be demonstrated clearly. Moreover, each distinct material is formed into the independent structural members to afford the load transmission in the design domain, due to the comparable values of Young’s modulus.

Table 5. The optimized results of the MBB beam with three materials

M2 material	2D-view of the TVF ϕ^1 at GQPs 	The optimized topology 
M3 material	2D-view of the TVF ϕ^2 at GQPs 	The optimized topology 
M4 material	2D-view of the TVF ϕ^3 at GQPs 	The optimized topology 
The TVFs ϕ^1, ϕ^2 and ϕ^3 at GQPs 		The TVFs ϕ^1, ϕ^2 and ϕ^3 in the design domain 
2D-view of the TVFs ϕ^1, ϕ^2 and ϕ^3 at GQPs 		The optimized topology 

Additionally, the convergent histories of the objective function and volume fractions for three materials are displayed in Fig. 12. It can be easily seen that all the iterative curves are very smooth and the optimization for three materials is featured with the high stability. The volume fractions of three TVFs can quickly arrive at the prescribed values, namely 20%, 12% and 3%. The corresponding volume fractions of the achieved topologies in Table 5 are equal to 20.13%, 11.5% and 2.98%, respectively. Hence, we can confirm that the M-ITO method has the capability to seek the optimized distributions of three materials.

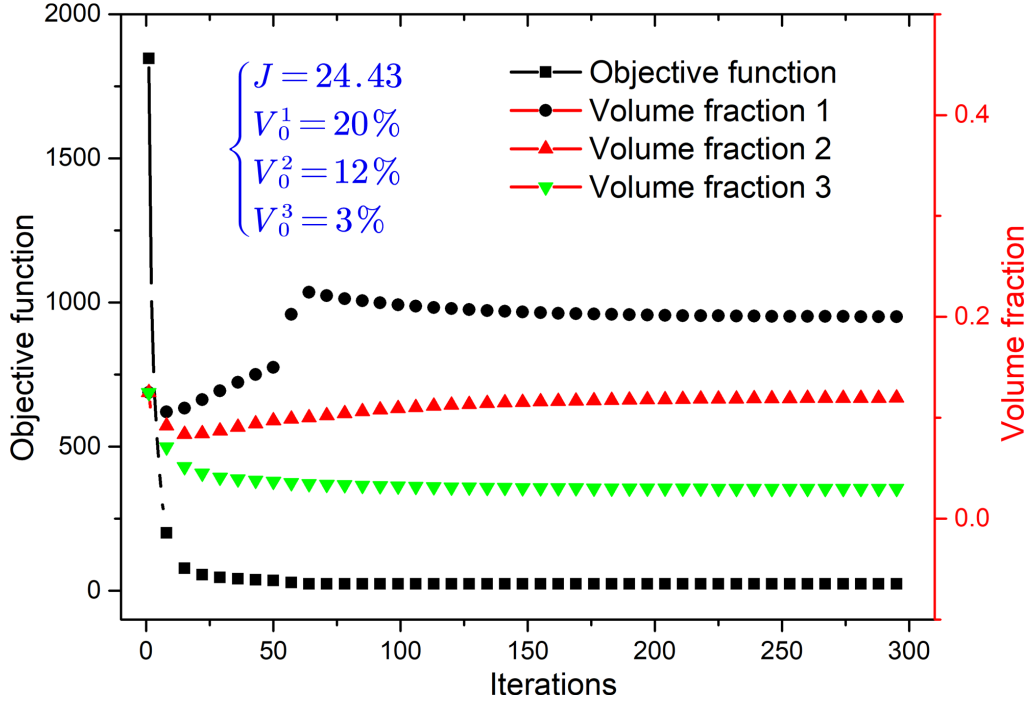


Fig. 12. Convergent histories

5.2 Cantilever beam

In this section, the cantilever beam will be optimized by the formulation 2 to study the effectiveness of the N-MMI model on the multi-material problem with the mass constraint. The structural design domain with the loads and boundary conditions is defined in Fig. 13, where the scales in two directions are 10 (L) and 5 (H), respectively. The cantilever beam is also parametrized by the NURBS surface, and the corresponding numerical details are listed below Fig. 13.

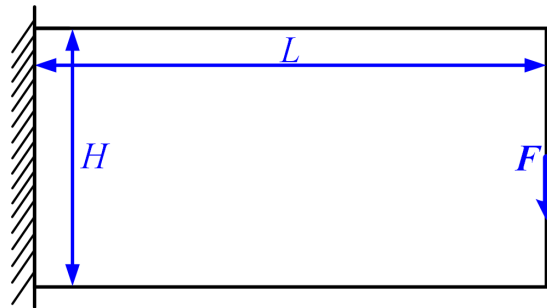


Fig. 13. Cantilever beam: IGA elements 100×50 ; $\Xi = \{0,0,0,0.01, \dots, 0.99,1,1,1\}$, $\mathcal{H} = \{0,0,0,0.02, \dots, 0.98,1,1,1\}$; $n = 102, m = 52$; $p = q = 2$.

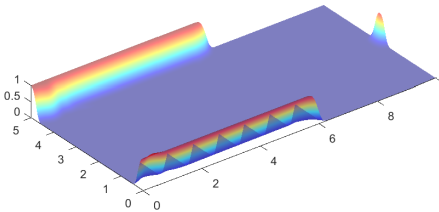
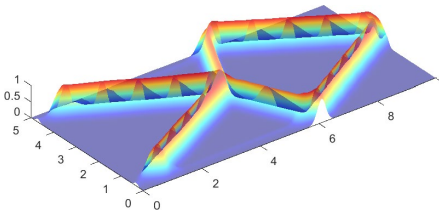
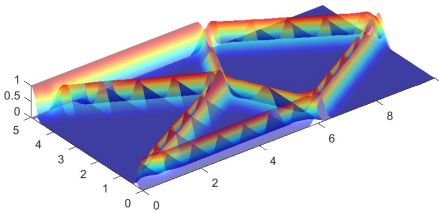
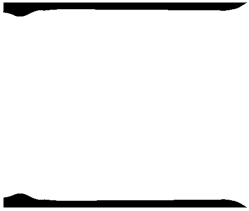
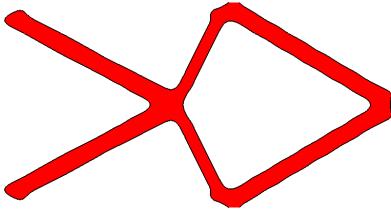
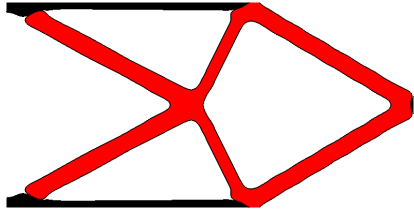
5.2.1 Two-material design

Two distinct materials (**M2** and **M3**) will be considered within the optimization of the cantilever beam. As defined in Table 3, **M2** material has the larger Young's modulus $E_0^2 = 10$, but with a lower Stiffness-to-mass ratio $\mathcal{R}_0^2 = 2$, compared to **M3** material with $E_0^2 = 5$ and $\mathcal{R}_0^2 = 2.5$ in Table 3. In formulation 2, the maximum consumption of the total mass G_m is set as 30. Similar to Section 5.2, two different colors

(the black and red) are used to show the overall distributions of **M2** and **M3** materials within the optimized design, respectively. The initial designs of the TVFs for two materials has the same densities in **Fig. 7**.

The optimized results of the cantilever beam with **M2** and **M3** materials are listed in **Table 6**. Firstly, the continuous distributions of the TVFs in the design domain are shown in the second row of **Table 6**. Similar to the above example in Section 5.1 for MBB beam, the distributions of the TVFs are also featured with the sufficient smoothness and continuity, which are beneficial to the latter definition of the structural topology. The heuristic scheme defined in Eq. (26) is applied to define the structural topology for multiple materials, where the constant is still set as 0.5. The topologies for two materials (**M2** and **M3**) are shown in the last row of **Table 6**. As given in the last row and column of **Table 6**, we can easily observe that the optimized distribution for two materials have the distinct interfaces and smooth boundaries between solids and voids. Hence, we can confirm that the N-MMI model is effective on the optimization of multi-material structures with the total mass constraint.

Table 6. The optimized results of cantilever beam with two materials

ϕ^1 in the design domain	ϕ^2 in the design domain	ϕ^1 and ϕ^2 in the design domain
		
The topology of M2 material	The topology of M3 material	The topology of cantilever beam
		

Meanwhile, **M2** and **M3** materials are formed into different structural members in the optimized topology to afford the loads, such as the black part filled with the strong **M2** material and the color area occupied by the weak **M3** material. Moreover, **M2** material is mainly filled in the areas having the stress concentration, in order to provide the higher stiffness for the beam. However, the weak material **M3** is dominant within the overall distribution, because the material has a larger stiffness-to-mass ratio. Hence, the formulation 2 with the total mass constraint improves the structural performance considering two components, namely the stiffness and mass, simultaneously. Finally, the iterative histories of the structural compliance, the total mass and mass of each material are shown in **Fig. 14 (a)**. Meanwhile, the iterative curves of the total volume fraction and the volume fraction for each material are displayed in **Fig. 14 (b)**. It can be easily seen that the

optimization with the total mass constraint for multiple materials is featured with the superior stability to seek the distributions of multiple materials in the design domain. Moreover, the mass of each material has been gradually adjusted during the optimization to enhance the structural performance as much as possible, rather than in a monotonous way of the single-material optimization.

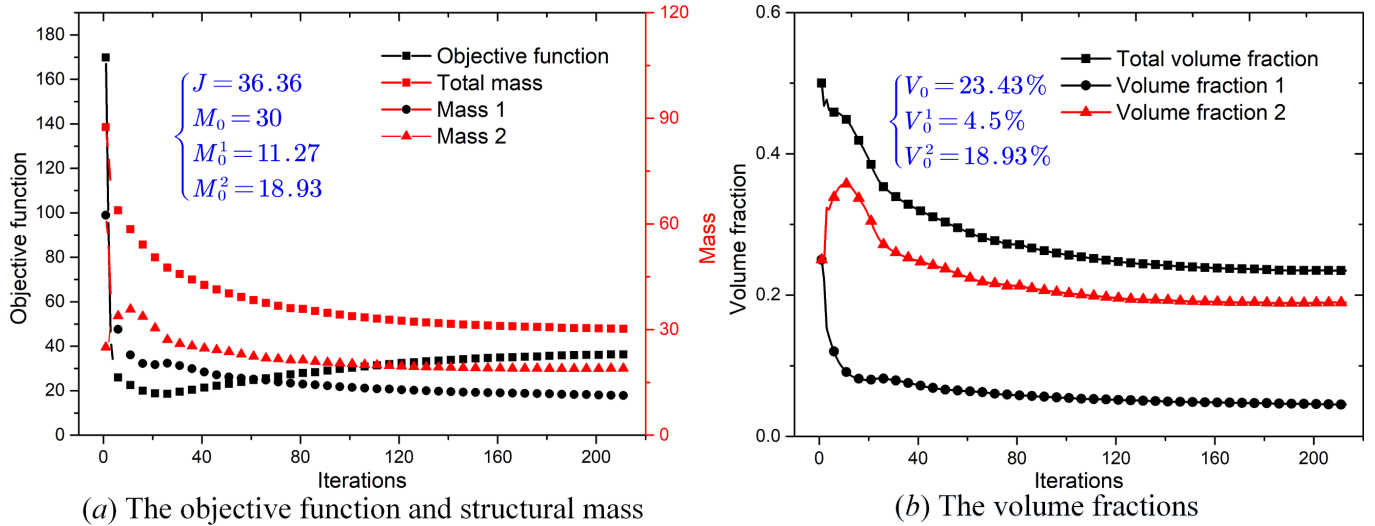


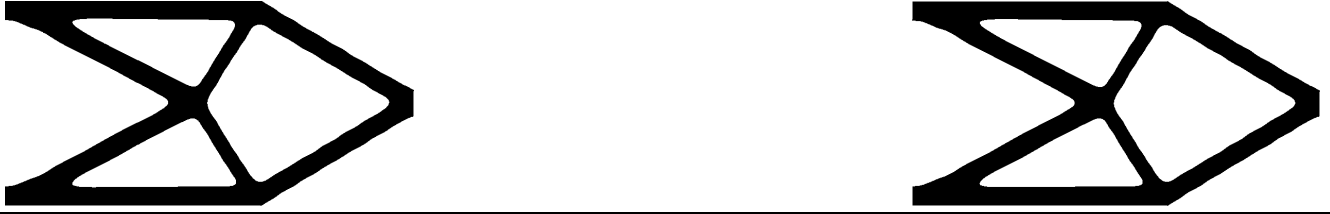
Fig. 14. Convergent histories

5.2.2 Influence of the stiffness-to-mass ratio

In order to show the influence of the stiffness-to-mass ratio on the multi-material optimization, **M1** and **M3** materials defined in **Table 3** are available in this case. The Young’s modulus $E_0^1 = 10$ and stiffness-to-mass ratio $\mathcal{R}_0^1 = 5$ of **M1** material are both larger than **M3** material having $E_0^3 = 5$ and $\mathcal{R}_0^3 = 2.5$. The total mass consumption is same as Section 5.2.1, namely $G_m = 30$. **M1** and **M3** materials are respectively plotted with the black and red. The initial designs of the TVFs for **M1** and **M3** materials are also consistent with Section 5.2.1, and with same densities in **Fig. 7**. As provided in **Table 7**, the optimized results of the cantilever beam with **M1** and **M3** materials are shown, including the TVFs in the design domain, the final topologies of **M1**, **M3** materials and the topology of the cantilever beam obtained by the heuristic scheme with the constant 0.5. It can be easily seen that the optimized topology of the cantilever beam with **M1** and **M3** materials is different from the solutions in Section 5.2.1.

Table 7. The optimized results of cantilever beam with two materials

ϕ^1 in the design domain	ϕ^2 in the design domain	ϕ^1 and ϕ^2 in the design domain
The topology of M1 material	The topology of M3 material	The topology of cantilever beam



In the current design, the cantilever beam only contains **M1** material, even if **M3** material is available in the optimization. As shown in **Fig. 15**, the mass of **M3** material gradually decreases during the optimization, until it arrives at zero. Meanwhile, the mass of **M1** material is equal to the total mass, and the corresponding curves coincide together. Hence, we confirm that the multi-material topology optimization formulation with the total mass constraint is more prone to choose the material with both the larger Young’s modulus and stiffness-to-mass ratio, to improve structural performance. Meanwhile, it can also reveal that the developed M-ITO method with the N-MMI model has the capability to seek for the design with only one material, if the Young’s modulus and stiffness-to-mass ratio are both larger compared with other available materials. The main reason originates from that the total mass constraint in formulation 2 is separate and linear with respect to topology variables, and also the N-MMI model has the decoupled and serial manner of design variables and topology variables. Moreover, the designs of the cantilever beam in above examples, like **Fig. 11**, **Table 4-7**, do not have the “mixture” materials. Hence, the N-MMI model has more effectiveness for the multi-material topology optimization problems.

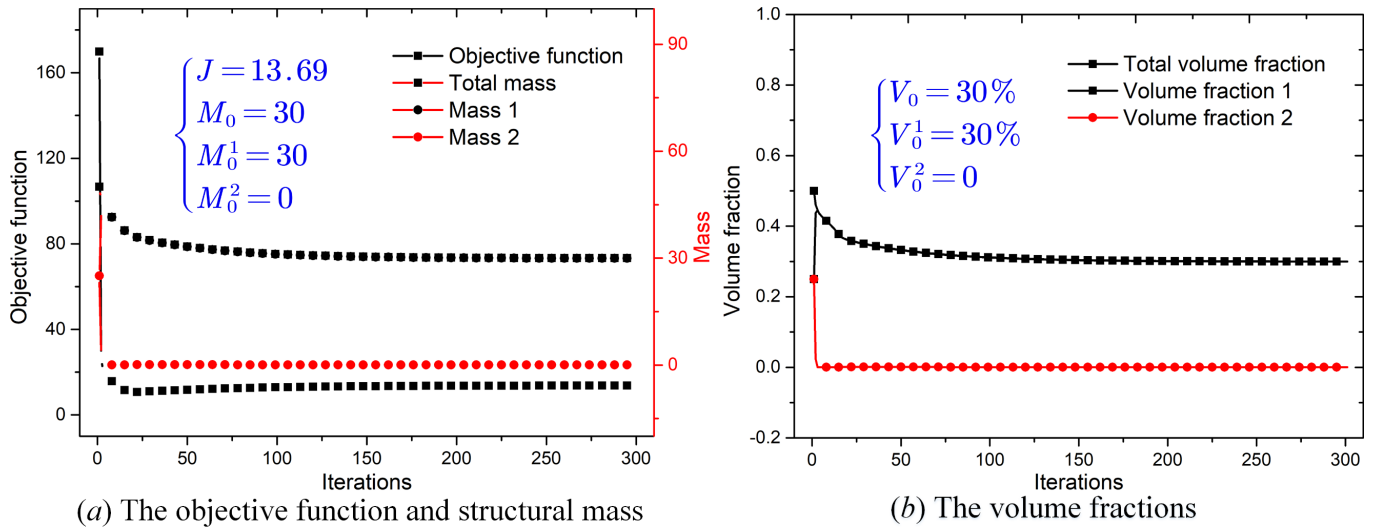


Fig. 15. Convergent histories

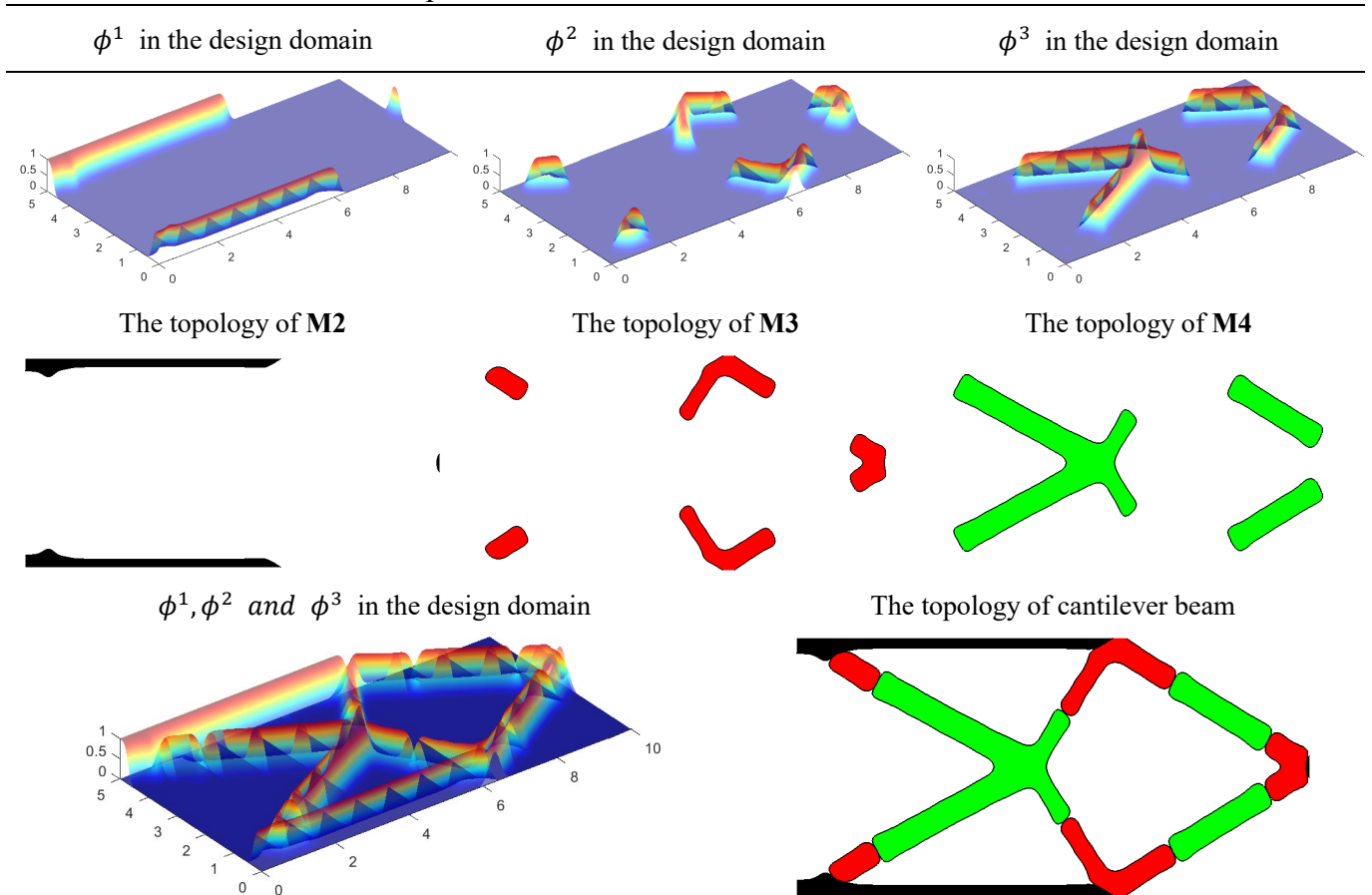
5.2.3 Three-material design

In this sub section, we will present the effectiveness of the formulation 2 to find the three-material design of the cantilever beam (**M2**, **M3** and **M4**). In **Table 3**, **M2** material has the larger Young’s modulus and a larger Stiffness-to-mass ratio is featured by **M3** material. Three materials (**M2**, **M3** and **M4**) will be plotted with different colors, namely the black, red and green colors, respectively, in the optimized distributions.

The maximum value of the total mass constraint is defined as 35. The initial designs of the TVFs for three materials have the same densities of the TVFs shown in Fig. 10.

The optimized results of the cantilever beam with three materials considering the total mass constraint are provided in Table 8. The continuous distributions of the TVFs in the design domain, the topologies of three different materials (M2, M3 and M4) and the topology of the cantilever beam are all included. It can be found that the optimized topology is featured with the smooth boundaries and distinct interfaces between solids and voids. Each material can constitute the independent structural members in the optimized topology to afford the imposed loads and boundary conditions, which shows the effectiveness of the M-ITO method to solve the multi-material problem with the total mass constraint. M2 material is also mainly filled in some regions with the occurrence of the stress concentration.

Table 8. The optimized results of cantilever beam with three materials



Finally, the iterative histories of the objective function, the total mass and mass of each material are shown in Fig. 16 (a), and Fig. 16 (b) displays the iterations for the total volume fraction and the volume fraction of each distinct material. We can find that the masses for M2, M3 and M3 materials are equal to 13.6, 8.2 and 13.2, respectively, and the volume fractions for them are 5.44%, 8.2% and 13.2%. Observed from the iterative curves, all the masses and volume fractions for three materials are changed in a non-monotonous

manner, and each of them is evolved to seek for an appropriate value in the optimization process, until the objective function arrives at $J = 34.73$.

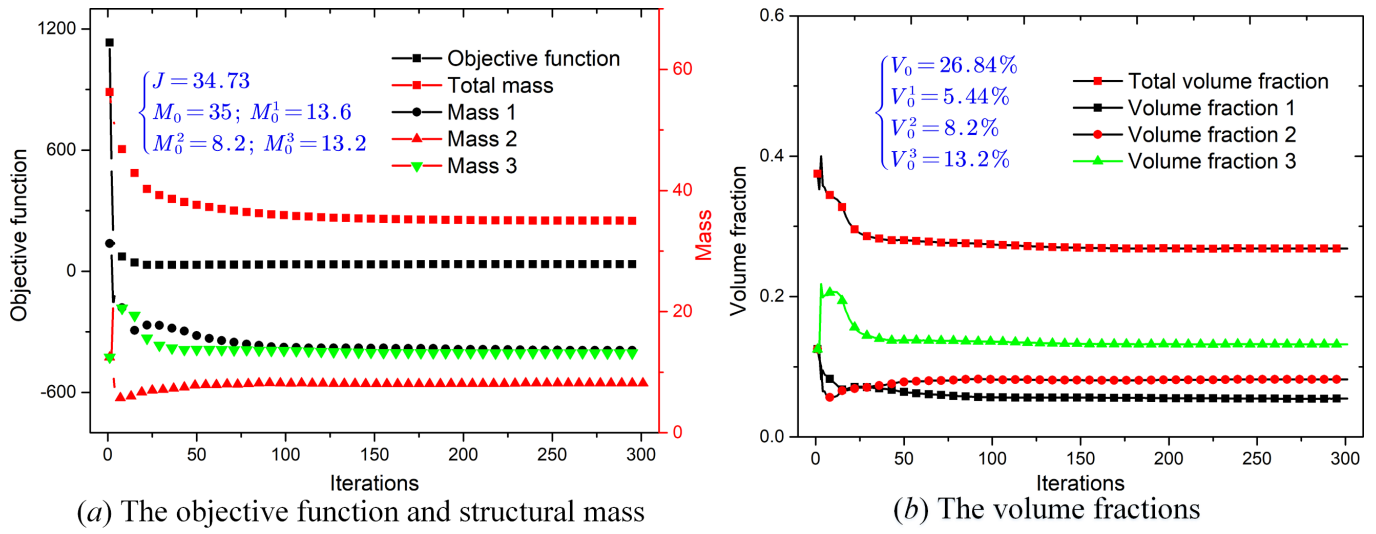


Fig. 16. Convergent histories

5.3 Quarter annulus

In this section, we intend to show the utility of the M-ITO formulation with multiple volume constraints on the optimization of the curved structures. In Fig. 17, a quarter annulus with loads and boundary conditions is defined, and two indices r and R are defined as 5 and 10, respectively. NURBS is used to construct the geometrical model and numerical analysis model of the quarter annulus. It should be noted that this example uses the cubic NURBS basis functions to model the structural geometry and construct the solution space, which is more beneficial to improve the numerical precision [48]. Meanwhile, this example will be studied in two cases. Case 1 performs the two-material design (M2 and M3) and case 2 considers three materials (M2, M3 and M4). In case 1, the maximum volume fractions for M2 and M3 materials are defined as 25% and 12%, respectively. In case 2, the maximum consumptions of M2, M3 and M4 materials are respectively set to be 25%, 10% and 5%. Three materials are plotted with the black, red and green colors, respectively. The initial designs of cases 1 and 2 have the same densities shown in Fig. 7 and Fig. 10, respectively.

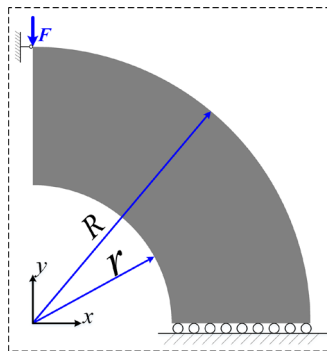
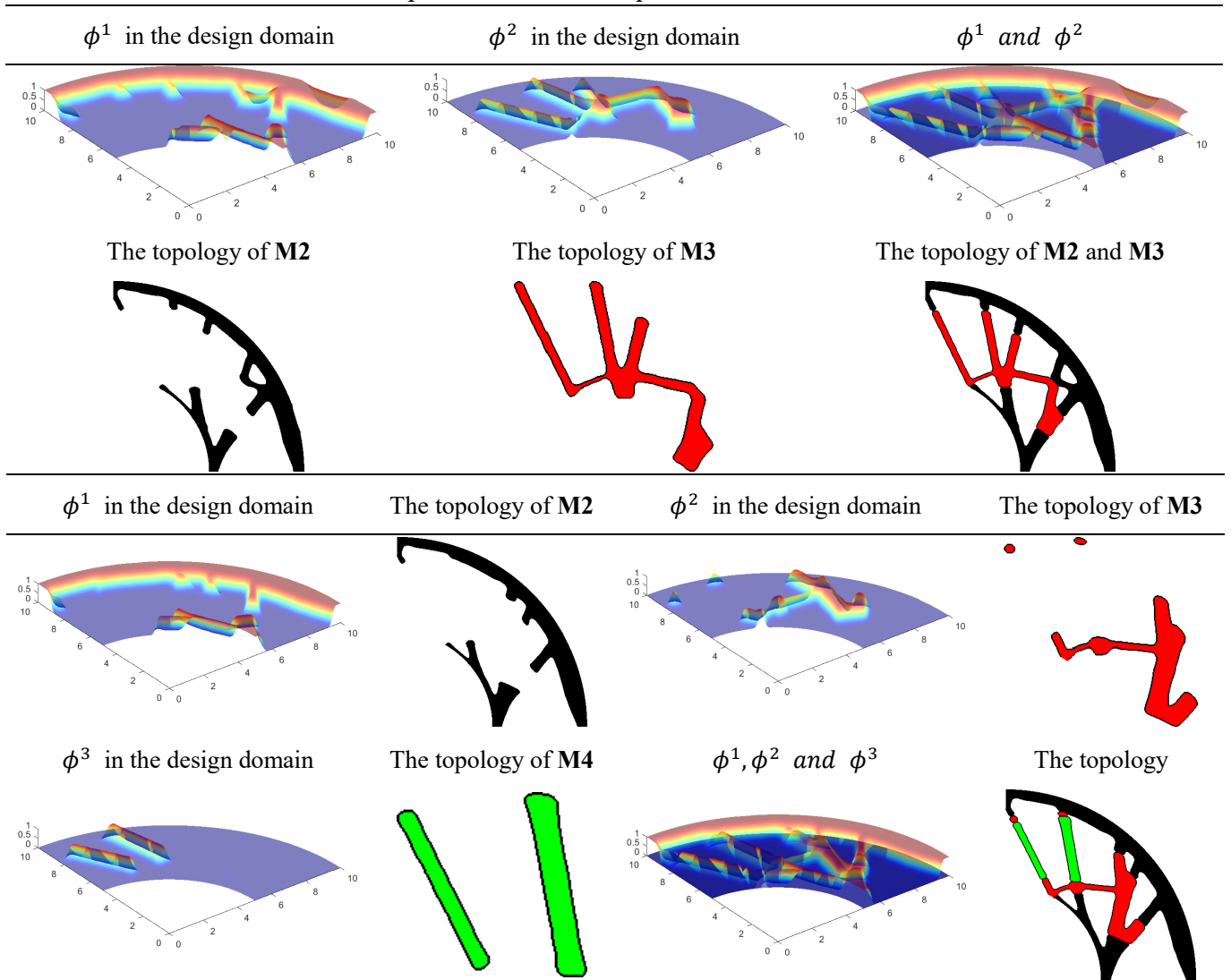


Fig. 17. Quarter annulus: IGA elements 100×50 ; $\Xi = \{0,0,0,0,0.01, \dots, 0.99,1,1,1,1\}$, $\mathcal{H} = \{0,0,0,0,0.02, \dots, 0.98,1,1,1,1\}$; $n = 103, m = 53$; $p = q = 3$.

The optimized results of the quarter annulus with **M2** and **M3** materials in case 1 are listed in **Table 9**, and which also provides the optimized results of the quarter annulus with **M2**, **M3** and **M4** materials. As we can see, the distributions of the TVFs in the design domain, the topologies for multiple materials and the topology of the quarter annulus are both presented. It can be easily found that the optimized topologies of the quarter annulus in cases 1 and 2 are both featured with the smooth structural boundaries and distinct interfaces between the solids and voids. No overlaps are occurred in the optimized topologies of the quarter annulus, which shows the effectiveness of the N-MMI model. Multiple materials can be formed into the independent parts of the topologies to play the respective roles to afford the imposed loads. The appropriate distributions of the distinct materials can demonstrate the effectiveness and utility of the developed M-ITO method on the optimization of the curved structures with multiple materials.

Table 9. The optimized results of quarter annulus in cases 1 and 2



5.4 3D Michell structure

This section will discuss the effectiveness of the M-ITO method on the optimization of 3D structures with multiple materials. As displayed in **Fig. 18**, a 3D Michell structure with the loads and boundary conditions

is defined. The quadratic NURBS basis functions are used to construct the NURBS solid and the numerical analysis model for the 3D Michell structure. The knot vectors and IGA elements are listed below **Fig. 18**. Meanwhile, this example will be also discussed in two cases, in which case 1 considers the optimization of two materials (**M2** and **M3** materials are available) in the design domain and case 2 intends to optimize the 3D Michell structure with **M2**, **M3** and **M4** materials. In case 1, the allowable material consumptions for **M2** and **M3** are defined as 14% and 6%, respectively. The maximum volume fractions of **M2**, **M3** and **M4** materials in case 2 are set as 16%, 3.5% and 2.5%, respectively. **M2**, **M3** and **M4** materials are also shown with the black, red and green colors, respectively. Additionally, the initial designs of cases 1 and 2 have the same densities of the TVFs shown in **Fig. 7** and **Fig. 10**, respectively.

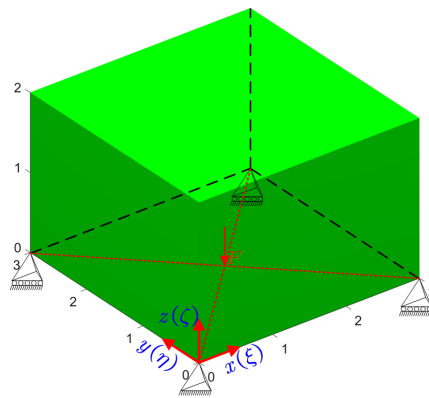
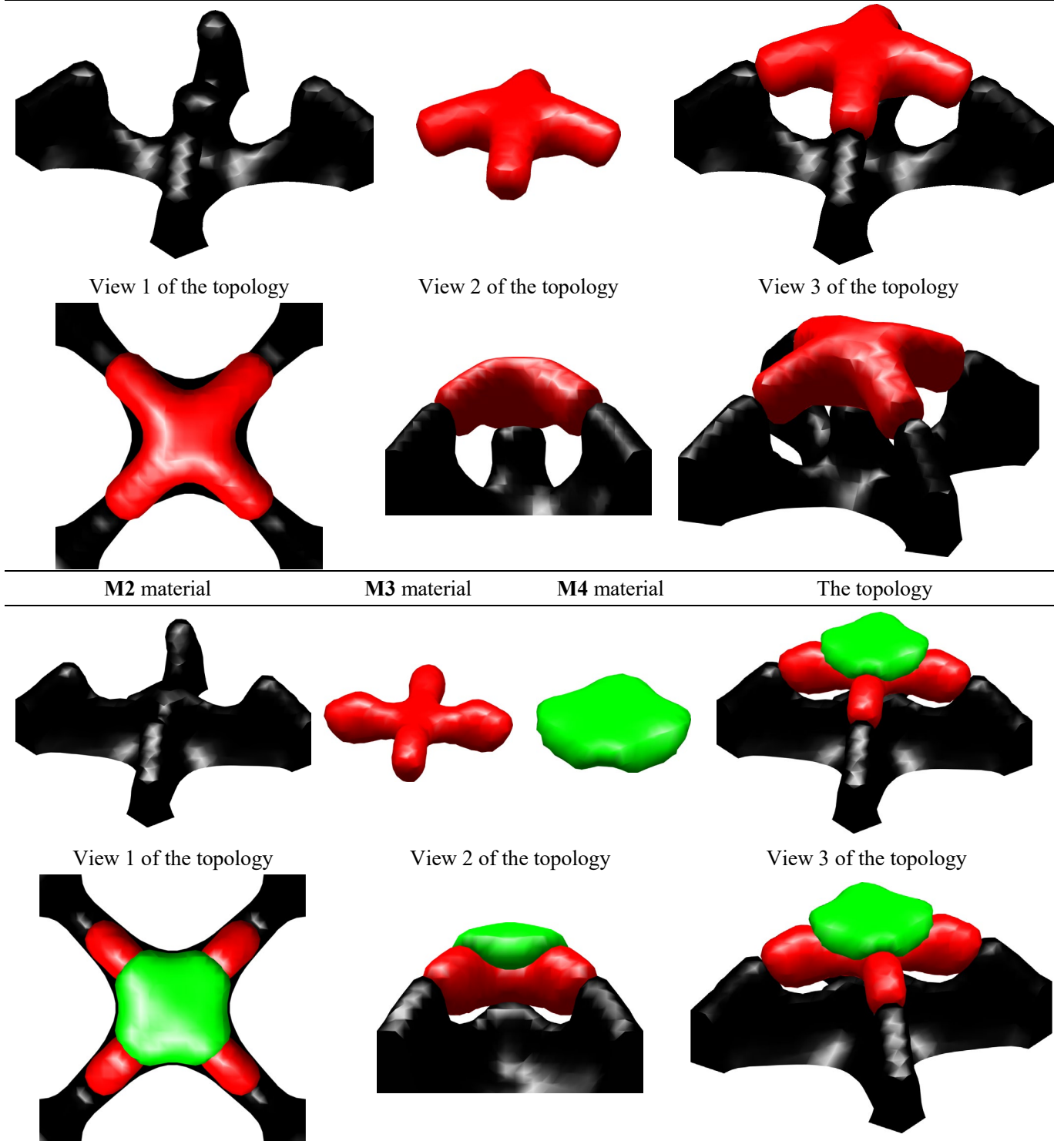


Fig. 18. 3D Michell structure: IGA elements $30 \times 30 \times 18$; $\Xi = \mathcal{H} = \{0,0,0,0.0333, \dots, 0.9667, 1, 1, 1\}$, $\mathcal{Z} = \{0,0,0,0.0556, \dots, 0.9444, 1, 1, 1\}$; $n = m = 32$, $l = 20$; $p = q = r = 2$.

In **Table 10**, the optimized results of the 3D Michell structure with **M2** and **M3** materials are provided, and the optimized results of the 3D Michell structure with three materials (**M2**, **M3** and **M4**) are also listed. As far as the 3D optimization, the DVFs and the TVFs correspond to the 4D functions, and it is hard to display the 4D data in a figure. Hence, we present the 3D-view of the TVFs with the higher values than the constant 0.5, and the corresponding topologies of **M2**, **M3** and **M4** materials. It can be easily seen that the optimized topologies of the 3D Michell structure with two materials and three materials are both featured with the smooth structural boundaries and distinct interfaces between different materials and void phases. The appropriate distributions of **M2**, **M3** and **M4** materials can be beneficial to afford the imposed loads and boundary conditions, which can constitute the independent structural members in the design domain. We also provide different views for the optimized topologies in two cases to present the geometrical features. Hence, the effectiveness of the developed M-ITO method with the N-MMI model for solving the 3D multi-material optimization can also be demonstrated.

Table 10. The optimized results of 3D Michell structure in two cases

M2 material	M3 material	The topology
--------------------	--------------------	--------------



6 Conclusions

In this paper, a more effective M-ITO method with the N-MMI model is proposed for the optimization of multiple materials distribution in structures. Firstly, the N-MMI model with the decoupled expression and serial evolving for design variables and topology variables is developed using NURBS, mainly involving the DVFs, TVFs, and the multi-material interpolation. Secondly, two M-ITO formulations are developed using the N-MMI model for two problems with multiple volume constraints and the total mass constraint, respectively, where IGA is applied to solve structural responses.

In numerical examples, two different M-ITO formulations are discussed in detail to demonstrate the more effectiveness of the N-MMI model in the multi-material optimization. The formulation considering multiple volume constraints is studied using the optimization of MBB beam with two and three materials, and the optimization of cantilever beam with two and three materials is applied to address the effectiveness of the M-ITO method on the problem with the total mass constraint. According to the numerical results, we can see that the proposed N-MMI model can effectively offer more benefits for the multi-material optimization, such as lower the numerical complexity and remove several numerical troubles. The M-ITO method also has more capability to solve the problems with more materials phase. Moreover, the effectiveness and utility of the M-ITO method on the rectangular and curved structures in 2D and 3D are also presented. Finally, in the developed M-ITO method, NURBS work as a basis to develop the IGA model and the N-MMI model, where the Lagrange polynomials will be ineffective in the current work.

Acknowledgments

This work was partially supported by the National Natural Science Foundation of China (51675196), the Australian Research Council (ARC) - Discovery Projects (160102491), the Natural Science Foundation of Hubei Province (2019CFA059), and the Program for HUST Academic Frontier Youth Team (2017QYTD04).

References

- [1] M.P. Bendsøe, O. Sigmund, *Topology Optimization: Theory, Methods and Applications*, (2003).
- [2] M. Bendsøe, N. Kikuchi, Generating optimal topologies in structural design using a homogenization method, *Comput Methods Appl Mech Eng.* 71 (1988) 197–224.
- [3] M. Zhou, G.I.N. Rozvany, The COC algorithm, Part II: Topological, geometrical and generalized shape optimization, *Comput. Methods Appl. Mech. Eng.* 89 (1991) 309–336.
- [4] M.P. Bendsøe, O. Sigmund, Material interpolation schemes in topology optimization, *Arch. Appl. Mech.* 69 (1999) 635–654.
- [5] Y.M. Xie, G.P. Steven, A simple evolutionary procedure for structural optimization, *Comput. Struct.* 49 (1993) 885–969.
- [6] J.A. Sethian, A. Wiegmann, Structural Boundary Design via Level Set and Immersed Interface Methods, *J. Comput. Phys.* 163 (2000) 489–528.
- [7] M.Y. Wang, X. Wang, D. Guo, A level set method for structural topology optimization, *Comput. Methods Appl. Mech. Eng.* 192 (2003) 227–246.
- [8] G. Allaire, F. Jouve, A.M. Toader, Structural optimization using sensitivity analysis and a level-set method, *J. Comput. Phys.* 194 (2004) 363–393.
- [9] J. Gao, H. Li, Z. Luo, L. Gao, P. Li, Topology optimization of micro-structured materials featured with the specific mechanical properties, *Int. J. Comput. Methods.* 15 (2018) 1850144.
- [10] S. Chu, L. Gao, M. Xiao, Z. Luo, H. Li, X. Gui, A new method based on adaptive volume constraint and stress penalty for stress-constrained topology optimization, *Struct. Multidiscip. Optim.* 57 (2018) 1163–1185.

- [11] S. Chu, L. Gao, M. Xiao, Z. Luo, H. Li, Stress-based multi-material topology optimization of compliant mechanisms, *Int. J. Numer. Methods Eng.* 113 (2018) 1021–1044.
- [12] J. Gao, H. Li, L. Gao, M. Xiao, Topological shape optimization of 3D micro-structured materials using energy-based homogenization method, *Adv. Eng. Softw.* 116 (2018) 89–102.
- [13] D. Li, W. Liao, N. Dai, G. Dong, Y. Tang, Y.M. Xie, Optimal design and modeling of gyroid-based functionally graded cellular structures for additive manufacturing, *Comput. Des.* 104 (2018) 87–99.
- [14] X. Zhang, A. Takezawa, Z. Kang, Robust topology optimization of vibrating structures considering random diffuse regions via a phase-field method, *Comput. Methods Appl. Mech. Eng.* 344 (2019) 766–797.
- [15] H. Wang, Q.-H. Qin, C.-Y. Lee, n-sided polygonal hybrid finite elements with unified fundamental solution kernels for topology optimization, *Appl. Math. Model.* 66 (2019) 97–117.
- [16] J. Gao, Z. Luo, H. Li, P. Li, L. Gao, Dynamic multiscale topology optimization for multi-regional micro-structured cellular composites, *Compos. Struct.* 211 (2019) 401–417.
- [17] Y. Zhang, M. Xiao, L. Gao, J. Gao, H. Li, Multiscale topology optimization for minimizing frequency responses of cellular composites with connectable graded microstructures, *Mech. Syst. Signal Process.* 135 (2020) 106369.
- [18] J. Thomsen, Topology optimization of structures composed of one or two materials, *Struct. Optim.* 5 (1992) 108–115.
- [19] O. Sigmund, S. Torquato, Design of materials with extreme thermal expansion using a three-phase topology optimization method, *J. Mech. Phys. Solids.* 45 (1997) 1037–1067.
- [20] L. V. Gibiansky, O. Sigmund, Multiphase composites with extremal bulk modulus, *J. Mech. Phys. Solids.* 48 (2000) 461–498.
- [21] O. Sigmund, Design of multiphysics actuators using topology optimization - Part II: Two-material structures, *Comput. Methods Appl. Mech. Eng.* 190 (2001) 6605–6627.
- [22] Y. Luo, Z. Kang, Layout design of reinforced concrete structures using two-material topology optimization with Drucker-Prager yield constraints, *Struct. Multidiscip. Optim.* 47 (2013) 95–110.
- [23] J. Stegmann, E. Lund, Discrete material optimization of general composite shell structures, *Int. J. Numer. Methods Eng.* 62 (2005) 2009–2027.
- [24] T. Gao, W. Zhang, A mass constraint formulation for structural topology optimization with multiphase materials, *Int. J. Numer. Methods Eng.* 88 (2011) 774–796.
- [25] T. Gao, P. Xu, W. Zhang, Topology optimization of thermo-elastic structures with multiple materials under mass constraint, *Comput. Struct.* 173 (2016) 150–160.
- [26] C.F. Hvejsel, E. Lund, Material interpolation schemes for unified topology and multi-material optimization, *Struct. Multidiscip. Optim.* 43 (2011) 811–825.
- [27] C.F. Hvejsel, E. Lund, M. Stolpe, Optimization strategies for discrete multi-material stiffness optimization, *Struct. Multidiscip. Optim.* 44 (2011) 149–163.
- [28] L. Yin, G.K. Ananthasuresh, Topology optimization of compliant mechanisms with multiple materials using a peak function material interpolation scheme, *Struct. Multidiscip. Optim.* 23 (2001) 49–62.
- [29] W. Zuo, K. Saitou, Multi-material topology optimization using ordered SIMP interpolation, *Struct. Multidiscip. Optim.* 55 (2017) 477–491.
- [30] R. Tavakoli, S.M. Mohseni, Alternating Active-Phase Algorithm for Multimaterial Topology Optimization Problems a 115-Line Matlab Implementation, *Struct. Multidiscip. Optim.* 49 (2014) 621–642.
- [31] E.D. Sanders, M.A. Aguiló, G.H. Paulino, Multi-material continuum topology optimization with arbitrary volume and mass constraints, *Comput. Methods Appl. Mech. Eng.* 340 (2018) 798–823.
- [32] M.Y. Wang, X. Wang, “Color” level sets: A multi-phase method for structural topology optimization with multiple materials, *Comput. Methods Appl. Mech. Eng.* 193 (2004) 469–496.
- [33] Y. Wang, Z. Luo, Z. Kang, N. Zhang, A multi-material level set-based topology and shape optimization method, *Comput. Methods Appl. Mech. Eng.* 283 (2015) 1570–1586.

- [34] A.H. Taheri, K. Suresh, An isogeometric approach to topology optimization of multi-material and functionally graded structures, *Int. J. Numer. Methods Eng.* 109 (2017) 668–696.
- [35] T.J.R. Hughes, *The finite element method: linear static and dynamic finite element analysis*, Courier Corporation, 2012.
- [36] T.J.R. Hughes, J.A.A. Cottrell, Y. Bazilevs, Isogeometric analysis: CAD, finite elements, NURBS, exact geometry and mesh refinement, *Comput. Methods Appl. Mech. Eng.* 194 (2005) 4135–4195.
- [37] J.A. Cottrell, T.J.R. Hughes, Y. Bazilevs, *Isogeometric Analysis: Toward Integration of CAD and FEA*, 2009.
- [38] J. Gu, T. Yu, L. Van Lich, T.-T. Nguyen, T.Q. Bui, Adaptive multi-patch isogeometric analysis based on locally refined B-splines, *Comput. Methods Appl. Mech. Eng.* 339 (2018) 704–738.
- [39] J. Gu, T. Yu, L. Van Lich, T.-T. Nguyen, S. Tanaka, T.Q. Bui, Multi-inclusions modeling by adaptive XIGA based on LR B-splines and multiple level sets, *Finite Elem. Anal. Des.* 148 (2018) 48–66.
- [40] Y.-D. Seo, H.-J. Kim, S.-K. Youn, Isogeometric topology optimization using trimmed spline surfaces, *Comput. Methods Appl. Mech. Eng.* 199 (2010) 3270–3296.
- [41] L. Dedè, M.J. Borden, T.J.R. Hughes, Isogeometric Analysis for Topology Optimization with a Phase Field Model, *Arch. Comput. Methods Eng.* 19 (2012) 427–465.
- [42] B. Hassani, M. Khanzadi, S.M. Tavakkoli, An isogeometrical approach to structural topology optimization by optimality criteria, *Struct. Multidiscip. Optim.* 45 (2012) 223–233.
- [43] X. Qian, Topology optimization in B-spline space, *Comput. Methods Appl. Mech. Eng.* 265 (2013) 15–35.
- [44] H.-Y. Lin, M. Rayasam, G. Subbarayan, ISOCOMP: Unified geometric and material composition for optimal topology design, *Struct. Multidiscip. Optim.* 51 (2015) 687–703.
- [45] Y. Wang, D.J. Benson, Isogeometric analysis for parameterized LSM-based structural topology optimization, *Comput. Mech.* 57 (2016) 19–35.
- [46] H.A. Jahangiry, S.M. Tavakkoli, An isogeometrical approach to structural level set topology optimization, *Comput. Methods Appl. Mech. Eng.* 319 (2017) 240–257.
- [47] H. Ghasemi, H.S. Park, T. Rabczuk, A level-set based IGA formulation for topology optimization of piezoelectric materials, *Comput. Methods Appl. Mech. Eng.* 313 (2017) 239–258.
- [48] J. Gao, L. Gao, Z. Luo, P. Li, Isogeometric topology optimization for continuum structures using density distribution function, *Int. J. Numer. Methods Eng.* 119 (2019) 991–1017.
- [49] J. Gao, H. Xue, L. Gao, Z. Luo, Topology optimization for auxetic metamaterials based on isogeometric analysis, *Comput. Methods Appl. Mech. Eng.* 352 (2019) 211–236.
- [50] Q.X. Lieu, J. Lee, A multi-resolution approach for multi-material topology optimization based on isogeometric analysis, *Comput. Methods Appl. Mech. Eng.* 323 (2017) 272–302.
- [51] L. Piegl, W. Tiller, *The NURBS Book*, *Comput. Des.* 28 (1996) 665–666.
- [52] C. de Boor, A practical guide to splines, *Math. Comput.* 34 (1980) 325.
- [53] K. Matsui, K. Terada, Continuous approximation of material distribution for topology optimization, *Int. J. Numer. Methods Eng.* 59 (2004) 1925–1944.
- [54] G.H. Paulino, C.H. Le, A modified Q4/Q4 element for topology optimization, *Struct. Multidiscip. Optim.* 37 (2009) 255–264.
- [55] Z. Kang, Y. Wang, Structural topology optimization based on non-local Shepard interpolation of density field, *Comput. Methods Appl. Mech. Eng.* 200 (2011) 3515–3525.
- [56] O. Sigmund, Morphology-based black and white filters for topology optimization, *Struct. Multidiscip. Optim.* 33 (2007) 401–424.
- [57] D. Shepard, A two-dimensional interpolation function for irregularly-spaced data, in: *Proc. 1968 23rd ACM Natl. Conf.*, ACM, 1968: pp. 517–524.
- [58] C. Wang, T. Yu, G. Shao, T.-T. Nguyen, T.Q. Bui, Shape optimization of structures with cutouts by an efficient approach based on XIGA and chaotic particle swarm optimization, *Eur. J. Mech. - A/Solids.* 74 (2019) 176–187.

- [59] S.H. Sun, T.T. Yu, T.T. Nguyen, E. Atroshchenko, T.Q. Bui, Structural shape optimization by IGABEM and particle swarm optimization algorithm, *Eng. Anal. Bound. Elem.* 88 (2018) 26–40.
- [60] K. Svanberg, The method of moving asymptotes - a new method for structural optimization, *Int. J. Numer. Methods Eng.* 24 (1987) 359–373.